Anisotropy Effects in a Dielectric Haloscope for Dark Matter Searches

Master Thesis in Physics

Submitted by:

Bernardo Ary dos Santos García

November 2021

Supervised by: Prof. Alexander Schmidt

Physics Institute III A

RWTH Aachen University

Declaration

I declare that the work contained in this thesis is my own, except where explicitly stated otherwise. In addition this work has not been submitted to obtain another degree or professional qualification.

Signed: _____

Date: _____

Acknowledgments

I would like to use this lines to give my gratitude to Alexander Schmidt, for his supervision in this thesis, and for giving me a very interesting topic to work on. To Dominik Bergermann who very kindly introduced me to the simulation code, and provided me with the optimized disc positions used throughout the thesis. Apart from this he also helped me by proofreading this thesis, as did Erdem Öz and Andrea Pérez, whose feedback was very helpful. Lastly I would like to thank my parents Carmen and José Bruno, who provided me with the opportunity of studying this master degree, and were always there for me in the good and bad moments.

Contents

Abstract

The mystery of dark matter and the violation of Charge and Parity conjugation symmetry (CP symmetry) in quantum chromodynamics (QCD) remain as two of the unsolved problems in physics today. The axion constitutes a promising solution to both these problems. The MADMAX collaboration aims to build a dielectric haloscope targeted to detect galactic dark mater axions in the mass range of $40 - 400\,\mu eV$. The dielectric haloscope consists of a series of dielectric discs and a mirror placed inside a strong homogeneous magnetic field that would produce the emission of coherent electromagnetic radiation with a frequency related to the mass of the axion. In this thesis we adapt the current simulations of this experimental concept, to include the effects of disc anisotropy.

Chapter 1

Introduction

The existence of dark matter has been one of the open questions about the nature of the universe since in 1933, the Swiss physicist Frank Zwicky obtained evidence of unobserved matter while studying the rotation curves of galaxies around the Coma cluster. Estimations from ΛCDM tell us that this type of matter constitutes 27% of the total mass-energy of the universe. So far however, experiments have failed to provide any type of direct evidence for its existence.

The axion, a light, scalar, and weakly interacting particle, proposed in 1977 to solve the strong CP problem (Charge and Parity conjugation) of quantum chromodynamics (QCD) through the Peccei Quinn mechanism, constitutes one of the strongest candidates to explain this enduring mystery.

Different experimental concepts have been suggested to detect the axion. One of these is the dielectric haloscope. It consists of a series of dielectric discs and a mirror placed inside a strong homogeneous magnetic field to stimulate the production of electromagnetic radiation from galactic axion dark matter through the Primakoff effect. In an effort to build such an experiment the **MA**gnetized **D**isc and **M**irror **A**xion e**X**periment (**MADMAX**) collaboration was born in 2017, with the goal of reaching the unexplored axion mass range $m_a = 40 - 400\,\mu eV$. One of the big challenges in MADMAX comes from simulating the experiment with realistic effects. In this thesis we present one step forward in this direction by including the effects of anisotropy in the dielectric discs.

Chapter 2

Theoretical Motivation

In this chapter we introduce the strong CP problem and the PQ mechanism as one of its proposed solutions. This mechanism implies the existence of a new, very light and weakly interacting scalar particle: the axion. Apart from solving the strong CP problem, the axion is also one of the strongest candidates to be part of the observed dark matter. This gives rise to new experimental concepts to detect these elusive particles such as the axion haloscope proposed by Pierre Sikivie and its evolution, the dielectric haloscope.

2.1 The Strong CP Problem and the PQ Mechanism

The Standard Model of particle physics contains a term in the Lagrangian that breaks CP symmetry:

$$\mathcal{L}_{SM} \supset \bar{\theta}\frac{g_s^2}{32\pi^2}G_a^{\mu\nu}\tilde{G}^{a\nu} \tag{2.1}$$

where G and $\tilde{G}$ are the gluonic field strength tensor and its dual, and $\bar{\theta}$ is an angular constant $\bar{\theta} \in (-\pi, \pi)$ which is composed of two parts:

$$\bar{\theta} =\mid \theta + arg(detM) \mid \tag{2.2}$$

The first term is related to the QCD vacuum while the second comes from the quark mass matrix. One of the implications of such CP violating term in the SM Lagrangian would be contributions to electric dipole moments (EDMs) in hadrons. The neutron in particular would have an EDM given by:

$$d_n = (2,4 \pm 1,0)\,\bar{\theta} \times 10^{-3}\,\text{e fm} \tag{2.3}$$

with e, the charge of the electron. Experimental efforts have been carried out since the 60's to look for such EDMs with no success. Actual experimental limits give us an upper bound $\mid d_n \mid < 3 \times 10^{-13}$ e fm [1], and hence:

$$\mid \bar{\theta} \mid < 1,3 \times 10^{-10} \tag{2.4}$$

This is an extremely small number for a parameter with contributions coming from seemingly unrelated origin. Why this value is so small is the so called "Strong CP problem". Different solutions to this fine tuning problem have been proposed during the years. One of the most elegant was proposed in 1977, by R. Peccei and H. Quinn [2]. In their paper, they proposed the introduction of a new $U(1)_{PQ}$ global symmetry, with a spontaneous symmetry breaking pattern at some energy scale of order f_a. Subsequently F. Wilczek [3] and S. Weinberg [4] independently noticed that such a spontaneously broken symmetry implies the existence of a pseudo-Nambu Goldstone mode which Wilczek named the axion after some detergent brand. After quantization, this corresponds to a scalar particle with negative parity and a non zero mass (hence the pseudo) of order $\mathcal{O}(m_\pi f_\pi / f_a)$.

Effectively this new symmetry can be thought of as $\bar{\theta}$ becoming a dynamical field:

$$\bar{\theta} \rightarrow \bar{\theta}(x,t) = \frac{a(x,t)}{f_a} \tag{2.5}$$

with $a(x,t)$ the new axion field and f_a the previously mentioned scale of the $U(1)_{PQ}$ symmetry breaking with a vacuum expectation value (VEV) that relaxes to zero. The properties of this new particle, such as the mass and the interaction constants with other particles, can be calculated with the help of a low energy effective field theory such as Chiral Perturbation theory [5]. In this sense, the mass of the axion can be written in terms of the the masses of the up and down quarks (m_u, m_d), as well as the mass of the neutral pion (m_π), and the pion decay constant f_π:

$$m_a = \frac{\sqrt{m_u m_d}}{(m_u + m_d)} \frac{m_\pi f_\pi}{f_a} = 5.70(6)(4)\, \mu eV \left(\frac{10^{12}\, GeV}{f_a} \right) \tag{2.6}$$

where the numbers in brackets refer to the uncertainties in the values of the up and down quarks. The coupling to other particles can also be calculated. Since the axion has the same quantum numbers as the neutral pion π^0, we can infer that it will also have the same interactions with other particles. We are especially interested in its interactions with photons $(a \rightarrow \gamma\gamma)$. This way, one can write an effective Lagrangian density describing this interaction given by:

$$\mathcal{L} = \frac{1}{4}F_{\mu\nu}F^{\mu\nu} - J^{\mu}A_{\mu} + \frac{1}{2}\partial_{\mu}a\partial^{\mu}a - \frac{1}{2}m_a^2a^2 - \frac{g_{a\gamma\gamma}}{4}F_{\mu\nu}\tilde{F}^{\mu\nu}a \tag{2.7}$$

and obtain the coupling $g_{a\gamma\gamma}$:

$$g_{a\gamma\gamma} = -\frac{\alpha}{2\pi f_a}C_{a\gamma\gamma} = -2,04(3)\times 10^{-16}\,GeV^{-1}\left(\frac{m_a}{1\,\mu eV}\right)C_{a\gamma\gamma} \tag{2.8}$$

$$C_{a\gamma\gamma} = \frac{\mathcal{E}}{\mathcal{N}} - 1,92(4) \tag{2.9}$$

with α the fine structure constant and $C_{a\gamma\gamma}$ of order ~ 1. The values $\mathcal{E}$ and $\mathcal{N}$ are respectively the electromagnetic (EM) and color anomalies, and depend on the specifics of the application of the PQ mechanism. These have different values for different models. Classical examples are the KSVZ model with $\mathcal{E}/\mathcal{N} = 0$ or the DFSZ model with $\mathcal{E}/\mathcal{N} = 8/3$. One can thus see that the only unknown parameter for a specific model is the PQ symmetry breaking scale, f_a.

2.2 Axion Dark Matter

Apart from solving the Strong CP problem, the axion's properties make it a great candidate for the DM of the Universe. They are electrically neutral, extremely stable and have a very small coupling constant to other particles, which makes them collisionless and non-relativistic (cold dark matter).

Measurements of the rotation curves of the Milky Way estimate that the galaxy is embedded in a large DM halo with density $\rho_{DM} \approx 0.39\,GeVcm^{-3}$ around the solar system [6]. Furthermore, the relative velocities of this DM particles are estimated to be of order $v_a \sim \mathcal{O}(10^{-3})$ and with an extremely small velocity dispersion. This means that it would be possible to envision an experiment in which axions are always present and we only need to make them interact with known SM particles. In 1983 P. Sikivie proposed a new experimental concept to detect such axion DM: the axion haloscope [7]. Before going deeper into this concept, it's interesting to point out other possible candidates for dark matter, particularly the ones known as axion like particles.

2.2.1 Axion Like Particles

In addition to the QCD axion emerging from the PQ mechanism, other extensions of the SM (e.g. string theory) include spontaneously broken U(1) symmetries. Much like in the PQ mechanism this spontaneous symmetry breaking also gives rise to pNG particles with a small mass and weak interactions with other particles. These particles are also strong DM candidates, whose phenomenology is similar to the one for QCD axions; however, they have nothing to do with the PQ mechanism. In a nutshell this means that the mass and the interaction constant of these particles with other particles like photons is not related. Examples of such axion like particles (ALPs) are Majorons, Familons or closed string axions [8]. We are motivated therefore not only to look for axions with the mass and coupling constant to photons predicted by the different QCD models, but also for any other particle whose mass and photon interaction constant are unrelated.

2.3 The Axion Haloscope

As we argued in the previous section, it seems that if we are looking for general ALPs through their interaction with photons, there are two free parameters: the mass of the axion, m_a and the coupling constant $g_{a\gamma\gamma}$. The parameter space (Figure 2.1) gives us an idea of the regions already covered by experiments and the ones still unexplored.

Different experimental concepts have been proposed to probe this parameter space [9]. These are limited by the properties of the axion. We are interested in axion DM. In this spirit, if ALPs make up all, or even a fraction of dark matter, our galaxy would be embedded in a bath of them, and we would only need to make them interact with known SM particles in order to detect them. One of these experimental concepts is the previously mentioned axion haloscope. This consists of a cavity permeated with a magnetic field that resonantly converts axions into photons when the mass of the axion is matched to the cavity's resonant frequency.

The ADMX collaboration [10] has led the way building such a cavity, being able to probe QCD axions in the few-μeV mass region. The mass range that this type of experiment can cover is however bound to a small region of the parameter space. The difficulties in extending this range are twofold. First, if one wants to explore regions of lower mass, one needs a bigger cavity and therefore a bigger magnet. On the other hand, for higher mass regions one needs a smaller cavity. This however translates into a smaller conversion power to photons and therefore, lower sensitivity.

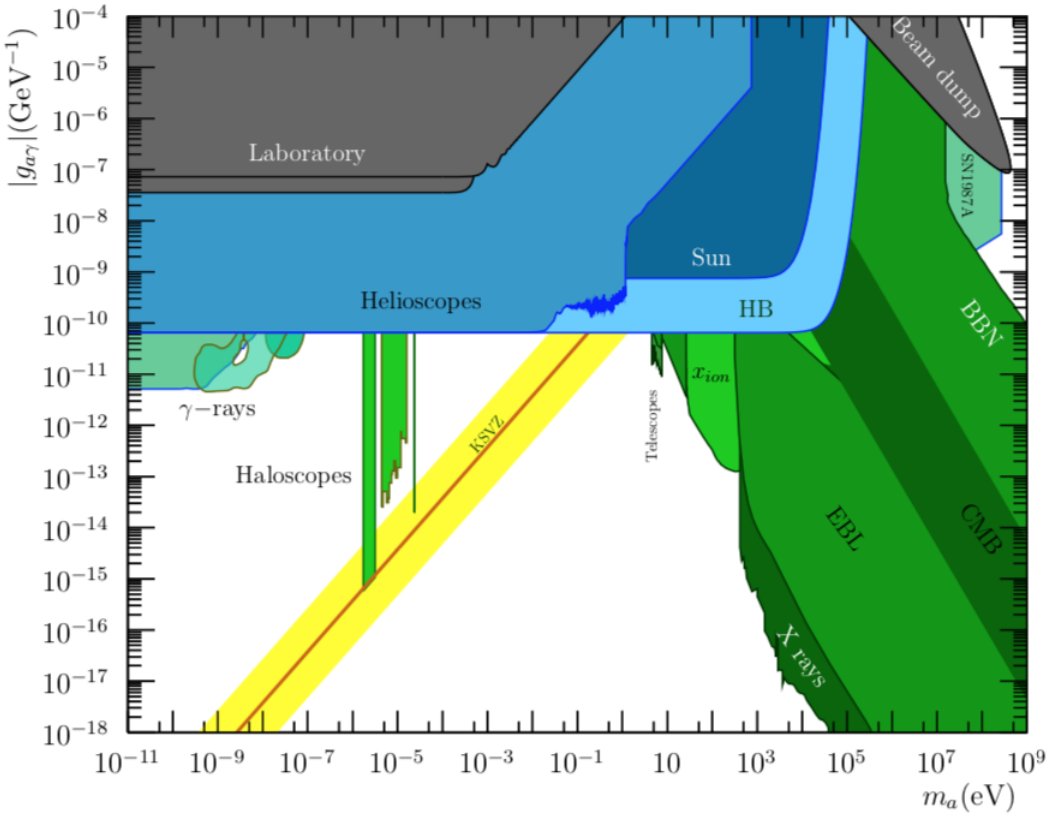

FIGURE 2.1: Constraints in the $m_a, g_{a\gamma\gamma}$ parameter space. In yellow the prediction of the different QCD models. The grey regions denote the constraints from laboratory searches, in blue for helioscope experiments and bounds from stellar physics, and in green for haloscopes and cosmology-dependent arguments. [9]

In an attempt to expand the search to other regions of the parameter space, the concept of dielectric haloscope was born [11] with the capability of exploring the $40 - 400\mu eV$ range. This is the main subject of the MADMAX collaboration. In the following chapter we will see what this concept consists of and how to simulate it.

Chapter 3

MADMAX and the Dielectric Haloscope

In this chapter the physical principles in play in the dielectric haloscope are reviewed. We start by understanding how an electric field can be induced in the presence of an external magnetic field and how the introduction of a series of parallel dielectric layers can boost the amplitude of this electric field. In order to calculate this amplitude one makes use of the so called transfer matrix formalism. The Boost factor, which is the amplification factor by which the amplitude is boosted, is introduced at the end of the chapter, as well as the simulation challenges of the experiment. For a complete derivation of the equations presented in this chapter: [11].

3.1 Linearized Maxwell's Equations

From the effective Lagrangian that describes the interaction between axions and photons (2.7), one obtains a set of modified Maxwell's equations:

$$\boldsymbol{\nabla} \cdot \boldsymbol{E} = \rho - g_{a\gamma} \boldsymbol{B} \cdot \boldsymbol{\nabla} a \tag{3.1a}$$

$$\boldsymbol{\nabla} \times \boldsymbol{B} - \dot{\boldsymbol{E}} = \boldsymbol{J} + g_{a\gamma}(\boldsymbol{B}\dot{a} - \boldsymbol{E} \times \boldsymbol{\nabla} a) \tag{3.1b}$$

$$\boldsymbol{\nabla} \cdot \boldsymbol{B} = 0 \tag{3.1c}$$

$$\boldsymbol{\nabla} \times \boldsymbol{E} + \dot{\boldsymbol{B}} = 0 \tag{3.1d}$$

$$\ddot{a} - \boldsymbol{\nabla}^2 a + m_a^2 a = g_{a\gamma} \boldsymbol{E} \cdot \boldsymbol{B} \tag{3.1e}$$

In the presence of a strong external magnetic field, $\boldsymbol{B}_e$ and assuming that the solutions of these equations are plane waves proportional to $e^{-i(\omega t - \boldsymbol{k}\cdot\boldsymbol{x})}$ one can write them in a

linearized form in Fourier space:

$$\epsilon \boldsymbol{k} \cdot \hat{\boldsymbol{E}} = -g_{a\gamma} \boldsymbol{k} \cdot \hat{\boldsymbol{B}}_{\boldsymbol{e}} \hat{a} \tag{3.2a}$$

$$\boldsymbol{k} \times \hat{\boldsymbol{H}} + \omega \epsilon \hat{\boldsymbol{E}} = -g_{a\gamma} \omega \boldsymbol{B}_{\boldsymbol{e}} \hat{a} \tag{3.2b}$$

$$\boldsymbol{k} \cdot \hat{\boldsymbol{B}} = 0 \tag{3.2c}$$

$$\boldsymbol{k} \times \hat{\boldsymbol{E}} - \omega \hat{\boldsymbol{B}} = 0 \tag{3.2d}$$

$$(\omega^2 - \boldsymbol{k}^2 - m_a^2)\hat{a} = -g_{a\gamma} \hat{\boldsymbol{E}} \cdot \boldsymbol{B}_{\boldsymbol{e}} \tag{3.2e}$$

with the hated quantities representing the complex amplitude of the fields and where ϵ is the dielectric constant of the medium, which we assume for the moment to be isotropic and linear.

Given that the value of $g_{a\gamma}$ is extremely small, one can also obtain from these modified Maxwell equations the dispersion relations for photons and axions to first order:

$$k_\gamma^2 = n^2 \omega_\gamma^2 \tag{3.3}$$

$$k_a^2 = \omega_a^2 - m_a^2 \tag{3.4}$$

with n being the refractive index $n^2 = \epsilon\mu$, and ϵ and μ respectively the dielectric constant and permeability of the medium. We will only deal with non-permeable media and so from now on we take $\mu = 1$ everywhere.

As mentioned in section 2.2 we are looking for CDM axions with a dispersion velocity $v_a \sim \mathcal{O}(10^{-3})$. This, added to the fact that the axion mass would be extremely small, translates into a large de Broglie wavelength given by:

$$\lambda_{dB} = 12.4\,\mathrm{m} \left(\frac{100\,\mu eV}{m_a} \right) \left(\frac{10^{-3}}{v_a} \right) \tag{3.5}$$

allowing us to treat the axion field as spatially homogeneous for small regions (i.e. $\boldsymbol{k}_a = 0$). One can therefore write the axion field as only a function of time:

$$a(t) = a_0 e^{-i\omega t} \tag{3.6}$$

with a_0 the amplitude of the field, and $\omega = m_a$ from the dispersion relation (3.4). Going back to equation (3.2b) the expression for the axion induced electric field becomes:

$$\boldsymbol{E}_a(t) = -\frac{\boldsymbol{E}_0}{\epsilon} e^{-i m_a t} \tag{3.7}$$

where we have introduced $\boldsymbol{E}_0 \equiv g_{a\gamma}\boldsymbol{B}_e a_0$ as a scale for the axion induced electric field.

3.2 Radiation from an Interface

Equation (3.7) is the essence of the haloscope concept. It tells us that if we have a strong magnetic field $\boldsymbol{B}_e$ in a medium with dielectric constant ϵ, then an electric field will be induced. This is known as the Primakoff effect. This axion induced electric field $\boldsymbol{E}_a$ is parallel to $\boldsymbol{B}_e$ and inversely proportional to ϵ. It's therefore easy to see, that if there is an interface between two media of different dielectric constant, that is parallel to this magnetic field, the axion induced electric field will be discontinuous. On the other hand, Maxwell's equations impose certain boundary conditions at this interface. In particular, since all the fields present in the system are parallel to this interface we only have:

$$\boldsymbol{E}_{\parallel,1} = \boldsymbol{E}_{\parallel,2} \qquad\qquad \boldsymbol{H}_{\parallel,1} = \boldsymbol{H}_{\parallel,2} \tag{3.8}$$

These boundary conditions are the same as in classical electrodynamics. The electric field condition comes from Faraday's law (3.1d) which is unchanged in the presence of axions. The magnetic field condition comes from Ampère's law (3.1b). The presence of axions gives an external volume current density, which is zero for a surface.

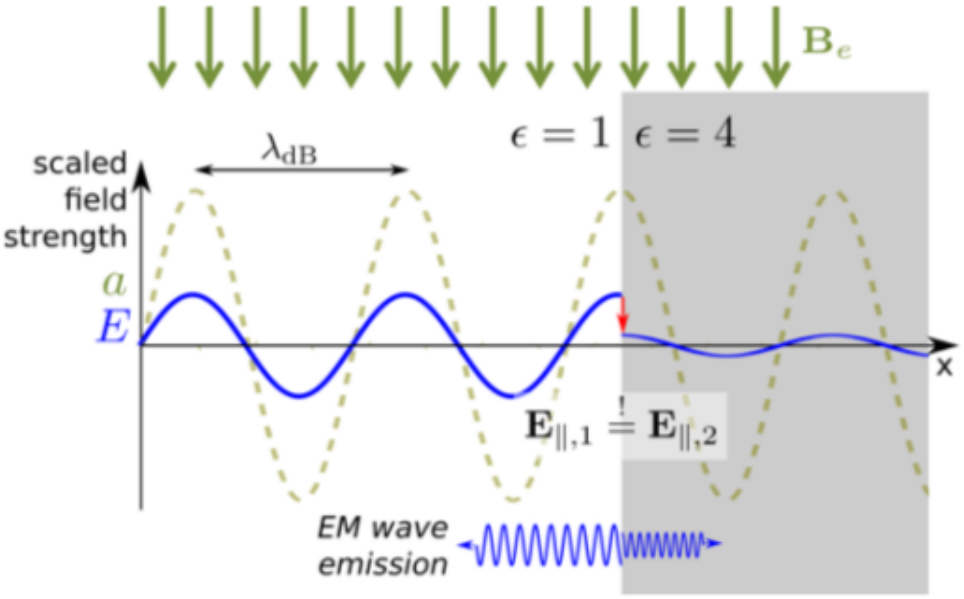

FIGURE 3.1: Representation of the axion photon conversion in an interface between different media of different dielectric constant ϵ, embedded in a strong homogeneous magnetic field. [11]

Satisfying the boundary conditions requires emission of EM radiation as sketched in Figure 3.1. To first approximation and for the sake of simplicity we will work in one dimension. This means that the interface between the two media is an infinite plane and the fields only vary in the spatial z-direction of Figure 3.1. The boundary conditions (3.8) can therefore be written in scalar form as:

$$E_{\gamma,1} + E_{a,1} = E_{\gamma,2} + E_{a,2} \qquad -\frac{\epsilon_1}{n_1} E_{\gamma,1} = \frac{\epsilon_2}{n_2} E_{\gamma,1} \tag{3.9}$$

with E_a the usual axion induced electric field and, E_γ and H_γ the electric and magnetic fields corresponding to the radiation emitted at the surface in order to fulfill the boundary conditions. These last amplitudes can hence be written in terms of the axion induced electric field as:

$$E_{\gamma,1} = (E_{a,2} - E_{a,1}) \frac{\epsilon_2 n_1}{\epsilon_1 n_2 + \epsilon_2 n_1} \tag{3.10a}$$

$$E_{\gamma,2} = -(E_{a,2} - E_{a,1}) \frac{\epsilon_1 n_2}{\epsilon_1 n_2 + \epsilon_2 n_1} \tag{3.10b}$$

$$H_{\gamma,(1/2)} = -(E_{a,2} - E_{a,1}) \frac{\epsilon_1 \epsilon_2}{\epsilon_1 n_2 + \epsilon_2 n_1} \tag{3.10c}$$

3.2.1 Power Emitted from a Mirror

One can now imagine the simple case of an interface between a perfect mirror ($\epsilon_1 = \infty$) and the vacuum ($\epsilon_2 = 1$). From the expressions in (3.10) one can calculate the amplitudes of the propagating waves for this case yielding: $E_{\gamma,2} = -E_{a,2}$. The cycle-averaged flux density in the z-direction is then given by:

$$\frac{P_\gamma}{A} = \frac{E_0^2}{2} = 2.2 \times 10^{-27} \frac{W}{m^2} \left(\frac{B_e}{10T} \right)^2 C_{a\gamma}^2 f_{DM} \tag{3.11}$$

where the factor f_{DM} represents the fraction of dark matter corresponding to axions. This is the so called dish antenna concept. The problem however, is that the power emitted by such an interface is too small to be observed with current technology. In order to amplify the signal one can place a set of dielectrics in front of this mirror: the dielectric haloscope. The radiation emitted by one of these interfaces interferes with the radiation coming from the other interfaces. One can thus try to place the different dielectrics in such a way so that the interference is constructive and the signal is amplified. To quantify this amplification we introduce the power boost factor, $\beta^2(\nu)$:

$$\frac{P_\gamma}{A} = \frac{E_0^2}{2} \quad \rightarrow \quad \frac{P_\gamma}{A} = \frac{\beta^2(\nu)E_0^2}{2} \tag{3.12}$$

which tells us how much the power that would be emitted by a single mirror is amplified in a dielectric haloscope. This can also be seen as β being the factor that quantifies the amplification of the amplitude, E_0 of the electric field (boost factor).

3.3 Dielectric Haloscope

The dielectric haloscope can be pictured as a setup with a series of $r = 0, .., m$ parallel regions such as the one in Figure 3.2. Each of these regions has a certain thickness and dielectric constant ϵ_r. In a dielectric haloscope, one typically has region, $r = 0$ as a perfect mirror (i.e. $\epsilon = \infty$) and a succession of vacuum and dielectric regions for $r = 1$ to $r = m$. Region $r = m$ will have an antenna which detects the total power generated by the system. For now however, we will treat this in the most general way, meaning every region has undefined parameters.

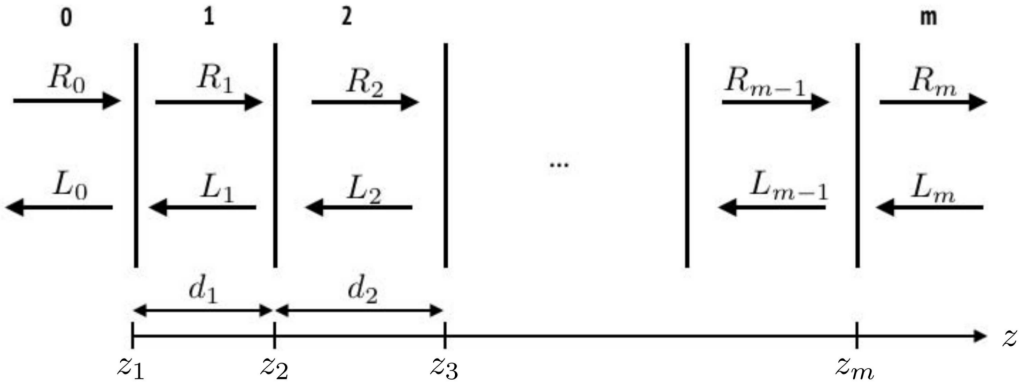

FIGURE 3.2: General setup of a dielectric haloscope with m regions r. [12]

The only fields inside the system are the axion induced electric field E_a and the EM waves emitted at each interface between the different media to compensate the discontinuity generated by E_a. In 1D these fields can be explicitly written as:

$$E_{a,r} = -A_r E_0 \qquad , \qquad A_r = \frac{1}{\epsilon_r}\frac{B_{e,r}}{B_{e,max}} \tag{3.13}$$

for the axion induced electric field, and:

$$E_r^R(z) = R_r e^{i\omega n_r \Delta z} \quad , \quad H_r^R(z) = \frac{\epsilon_r}{n_r} R_r e^{i\omega n_r \Delta z} \tag{3.14a}$$

$$E_r^L(z) = L_r e^{i\omega n_r \Delta z} \quad , \quad H_r^L(z) = -\frac{\epsilon_r}{n_r} L_r e^{i\omega n_r \Delta z} \tag{3.14b}$$

for the right and left moving components of the induced EM waves respectively. From now on we omit the time dependence $e^{-im_a t}$ which is the same for every field. One can now write the total fields in each region as the superposition of (3.13) and (3.14):

$$E_r^{tot}(z) = E_r^a + R_r e^{i\omega n_r \Delta z} + L_r e^{-i\omega n_r \Delta z} \tag{3.15a}$$

$$H_r^{tot}(z) = \frac{\epsilon_r}{n_r}\left(R_r e^{i\omega n_r \Delta z} - L_r e^{-i\omega n_r \Delta z}\right) \tag{3.15b}$$

In order to find the values of R_r and L_r we impose the continuity conditions (3.8) which at the interface, z_r are: $E_r(z_{r+1}) = E_{r+1}(z_{r+1})$ and $H_r(z_{r+1}) = H_{r+1}(z_{r+1})$. Substituting the total fields from (3.15) we find:

$$-E_0 A_r + R_r e^{i\delta_r} + L_r e^{-i\delta_r} = -E_0 A_{r+1} + R_{r+1} + L_{r+1} \tag{3.16a}$$

$$\frac{\epsilon_r}{n_r}\left(R_r e^{i\delta_r} - L_r e^{-i\delta_r}\right) = \frac{\epsilon_{r+1}}{n_{r+1}}\left(R_{r+1} - L_{r+1}\right) \tag{3.16b}$$

where δ_r is defined as the optical thickness:

$$\delta_r \equiv \omega n_r (z_{r+1} - z_r) \tag{3.17}$$

In order to solve these equations we make use of the transfer matrix formalism presented in the following section.

3.4 Transfer Matrix Formalism

The transfer matrix formalism allows us to obtain the solution to the set of equations in (3.16). These can be expressed in matrix form as:

$$\begin{pmatrix} R_{r+1} \\ L_{r+1} \end{pmatrix} = G_r P_r \begin{pmatrix} R_r \\ L_r \end{pmatrix} + E_0 S_r \begin{pmatrix} 1 \\ 1 \end{pmatrix} \tag{3.18}$$

where G_r, P_r and S_r are 2×2 matrices given by:

$$G_r = \frac{1}{2n_{r+1}} \begin{pmatrix} n_{r+1} + n_r & n_{r+1} - n_r \\ n_{r+1} - n_r & n_{r+1} + n_r \end{pmatrix} \tag{3.19}$$

$$P_r = \begin{pmatrix} e^{i\delta_r} & 0 \\ 0 & e^{-i\delta_r} \end{pmatrix} \tag{3.20}$$

$$S_r = \frac{A_{r+1} - A_r}{2} \begin{pmatrix} 1 & 0 \\ 0 & 1 \end{pmatrix} \tag{3.21}$$

Using these identities one can iterate the relation between the amplitude of any two regions in the system. Of particular interest to us is to have a relationship between the amplitudes of the fields in regions $r = 0$ and $r = m$. This relationship is given by:

$$\begin{pmatrix} R_m \\ L_m \end{pmatrix} = T \begin{pmatrix} R_0 \\ L_0 \end{pmatrix} + E_0 M \begin{pmatrix} 1 \\ 1 \end{pmatrix} \tag{3.22}$$

with T and M defined as:

$$T = T_0^m = G_{m-1} P_{m-1} G_{m-2} P_{m-2} ... G_0 P_0 \qquad , \qquad M = \sum_{s=1}^{m} T_s^m S_{s-1} \tag{3.23}$$

The dielectric constant (and therefore refractive index), the spacing between interfaces and the strength of the magnetic field are all known quantities. We are thus left with a system of two equations and four unknown variables. In order to obtain the solutions to the system one needs to impose certain initial conditions. We are particularly interested in two configurations of our general setup which will define two important quantities: Boost factor and Reflectivity.

3.4.1 Boost Factor

In the first scenario we imagine a system in which there are no incoming waves. This means we have $R_0 = L_m = 0$. From equation (3.22) one can calculate the left and right moving amplitudes in regions $r = 0$ and $r = m$:

$$L_0 = -E_0 \frac{M[2,1] + M[2,2]}{T[2,2]} \tag{3.24a}$$

$$R_m = E_0 \left(M[1,1] + M[1,2] - \frac{M[2,1] + M[2,2]}{T[2,2]} T[1,2] \right) \tag{3.24b}$$

In the booster one has a mirror in one of the extremes. Setting this region to be $r = 0$ and noticing that the dielectric constant for a mirror is $\epsilon_0 = \infty$ we are left with:

$$R_m = E_0 \left(M[1,1] + M[2,2] \right) \tag{3.25}$$

This is indeed the amplitude one measures when placing a receiver in region $r = m$.

As mentioned before, the boost factor is the factor that amplifies the amplitude emitted by a single mirror (i.e. E_0). This gives us a way to calculate it as:

$$\beta = \frac{R_m}{E_0} = M[1,1] + M[2,2] \tag{3.26}$$

3.4.2 Reflectivity and Group Delay

Apart from the boost factor one can also define the reflectivity of the system. To do so, suppose that there's no magnetic field. In that case the matrix formalism relates incoming and outgoing EM waves. One can therefore find:

$$\mathcal{R}_L = \left. \frac{L_0}{R_0} \right|_{L_m=0} = -\frac{T[2,1]}{T[2,2]} \tag{3.27a}$$

$$\mathcal{R}_R = \left. \frac{R_m}{L_m} \right|_{R_0=0} = \frac{T[1,2]}{T[2,2]} \tag{3.27b}$$

This quantity is related to the boost factor and doesn't require the existence of an axion to be measured, constituting therefore a good way of testing and calibrating the system.

3.4.3 The Area Law

At this point, the strategy to detect the axion seems clear enough. One places a strong homogeneous magnetic field in the haloscope and tries to position the dielectric discs so that there is constructive interference and the axion induced field is boosted. There's however a caveat: we don't know the mass of the axion. This is quite obvious but it also means the frequency of the photons produced by the Primakoff effect are unknown, and therefore the correct disc configuration that would boost the signal. One must hence scan through a large frequency range. This can be very time consuming, especially considering that to make a measurement with enough signal takes around a day's time. It turns out however that the boost factor has an important property known as the area law:

$$< |\mathcal{B}|^2 >_d = < |\mathcal{B}|^2 >_\nu \tag{3.28}$$

with $< ... >_d$ the average over all disc configurations and $< ... >_\nu$ the average over all frequencies. This tells us that we may choose between having high boost factor at a certain frequency or less boost for a larger frequency range.

One can therefore look for configurations where the boost factor curve covers a broad band and therefore, the disc positions need to be changed less frequently. Such broad band configurations are of the order of MHz.

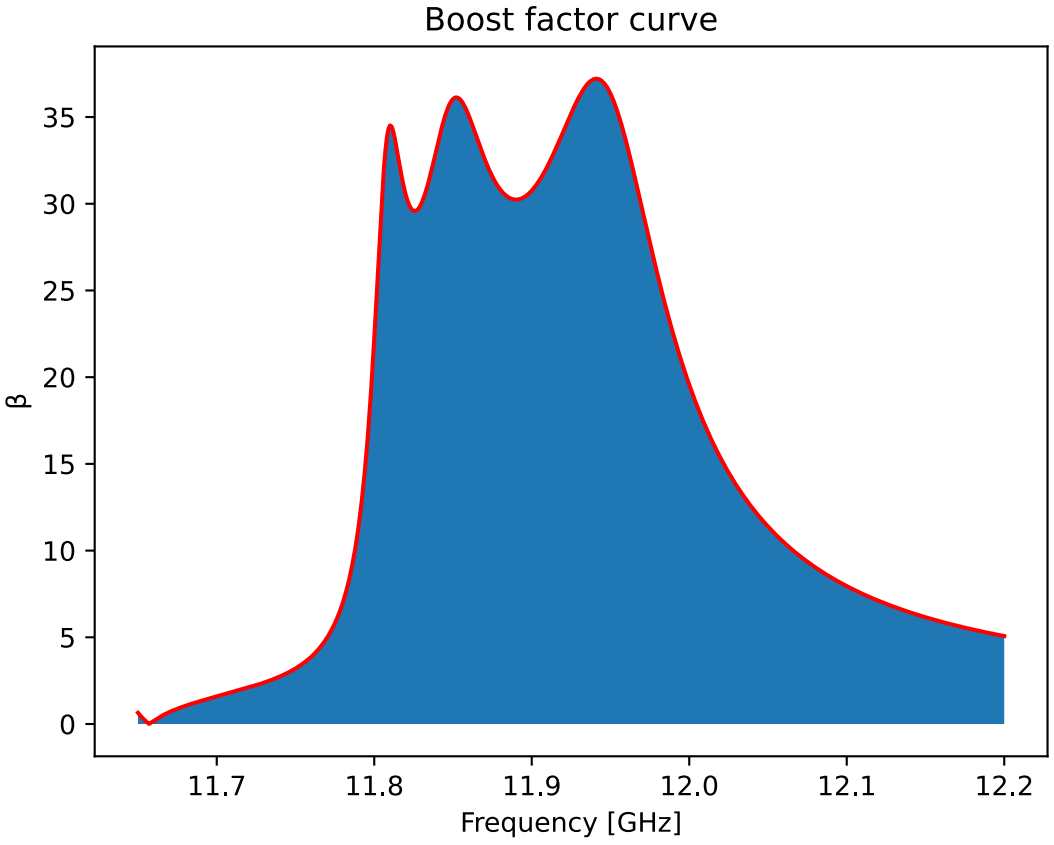

FIGURE 3.3: Example of a broad band 150 MHz boost factor curve.

3.5 Simulation Motivation

So far we have reviewed how to obtain the boost factor for a 1D dielectric haloscope. Simulations have been done to offer a 1D and 3D description of the system. This however has been done under many assumptions for the sake of simplicity. Effects such

as disc tilting, disc roughness and nonplanarity have been studied, leading to significant effects in the shape of the boost factor curve [12]. One of the assumptions in previous simulations is that our discs have an isotropic dielectric constant. This will be true for materials like lanthanum aluminate ($LaAlO_3$), but isn't the case for other materials e.g. sapphire (Al_2O_3). Although not the first choice because of its significantly lower dielectric constant ($\epsilon_{sapphire} \sim 9$ vs $\epsilon_{LaAlO_3} \sim 24$) it seems unrealistic that we will be able to have $1\,\mathrm{m}^2$ discs of lanthanum aluminate. It is therefore important that one understands the effects of anisotropy in the simulation. This is the main purpose of this thesis and the subject of the following chapters. In Chapter 4 a small review of electromagnetism in anisotropic media is done followed by the implementation of these effects in Chapter 5. This results in the modification of the transfer matrix formalism in order to include the effects of anisotropy. The results of the simulations with the anisotropic correction are presented in Chapter 6.

Chapter 4

Anisotropic Media

In this chapter some of the basic concepts and nomenclature of electromagnetism in anisotropic media are reviewed. This allows for a completely general description of any dielectric, with the familiar case of isotropic media as a special limit. The main novelties will be the treatment of the dielectric constant ϵ as a tensor $\bar{\bar{\epsilon}}$ and a new term in the wave equation. At the end of the chapter, the particular case of sapphire is described, as it is one of the most likely candidate materials for the discs in the experiment. For a more complete review on the physics of anisotropic media: [13]

4.1 Polarization Vector

Generally one can characterize materials in two large groups: conductors and dielectrics. In conductors, the electrons are free to move around the material, whereas in dielectrics, the electrons are bound to the atoms or molecules. This results in a different response when applying an external electric field to these two classes of materials. For dielectrics, our case of interest, this external electric field produces a redistribution of charges. The effect of this redistribution is captured by the Polarization vector $\boldsymbol{P}$ given, in natural units, by:

$$\boldsymbol{P} = \chi \boldsymbol{E} \tag{4.1}$$

with χ the electric susceptibility of the dielectric, ϵ_0 the dielectric constant, and $\boldsymbol{E}$ the external electric field. This is the simplest way of expressing the relation between polarization and electric field. When doing so we are however making a set of assumptions. First, we are ignoring any frequency dependence. Second, we are assuming that there are no non-linear effects. And finally we are assuming that the charge redistribution is parallel to the direction of the electric field. We are particularly interested in this last

one. Indeed this is what happens when the material in question is isotropic. For most materials however, the microscopic properties, be it molecular shape or even more clearly in the case of crystals, lattice symmetries, the charges may be displaced easier in certain directions than others. Hence, the polarization vector will not necessarily be parallel to the external electric field. One may think of this as the electric field inducing dipoles with certain preferred directions. These materials are known as anisotropic materials. In order to include this anisotropic behaviour, we may generalize the susceptibility χ to a rank 2 tensor $\bar{\bar{\chi}}$. Thus, the polarization vector is given by:

$$\boldsymbol{P} = \bar{\bar{\chi}}\boldsymbol{E} \tag{4.2}$$

In electromagnetism it is usual to use the displacement vector to include the effects of polarization. We can now write it for a general anisotropic medium as:

$$\boldsymbol{D} = (\mathbb{1} + \bar{\bar{\chi}})\boldsymbol{E} = \bar{\bar{\epsilon}}\boldsymbol{E} \tag{4.3}$$

where we have defined the dielectric tensor $\bar{\bar{\epsilon}} \equiv \mathbb{1} + \bar{\bar{\chi}}$.

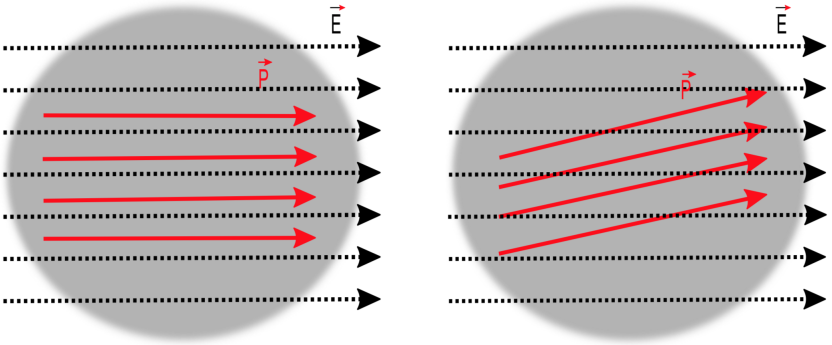

FIGURE 4.1: Representation of the polarization vector in isotropic media (left) and anisotropic media (right), embedded in an electric field.

Medium anisotropy also has affects in the Magnetization of the medium. These effects are however very small and can be neglected in the following discussion. For this reason we can express the relationship between magnetic fields $\boldsymbol{B}$ and magnetic field strengths $\boldsymbol{H}$ in the usual way:

$$\boldsymbol{B} = \mu\boldsymbol{H} \tag{4.4}$$

with the permeability of the medium μ as a scalar. The dielectric tensor is therefore the only change one has to consider when working with anisotropic media. We now proceed to discuss its most important properties.

4.2 Dielectric Tensor and Crystal Classes

From energy conservation arguments, it can be shown that for any dielectric, the dielectric tensor defined in (4.3) is symmetric. Hence, one can always find a reference frame in which this tensor is diagonal:

$$\bar{\bar{\epsilon}} = \begin{pmatrix} \epsilon_x & 0 & 0 \\ 0 & \epsilon_y & 0 \\ 0 & 0 & \epsilon_z \end{pmatrix} \tag{4.5}$$

This reference frame is known as the principal axes system. The components of this tensor ϵ_x, ϵ_y and ϵ_z, are the dielectric constants in the x, y and z directions. We will use this system mostly for its simplicity. In particular, because for a known electric field the displacement vector can easily be obtained:

$$\begin{aligned} D_x &= \epsilon_x E_x \\ D_y &= \epsilon_y E_y \\ D_z &= \epsilon_z E_z \end{aligned} \tag{4.6}$$

It also gives us a way of characterizing the different types of anisotropic materials. One can distinguish between three different types of materials:

- ***Isotropic***: These have only one independent element i.e. $\epsilon_x = \epsilon_y = \epsilon_z$, and the principal axes can be any set of orthogonal axes. Examples are the previously mentioned lanthanum aluminate, sodium chloride or diamond.
- ***Uniaxial***: These media have two independent elements i.e. $\epsilon_x = \epsilon_y \neq \epsilon_z$. Hence, to build the principal axes, one must find the direction for which the dielectric constant is ϵ_z. The remaining axes are any two orthogonal directions in the normal plane to the direction of ϵ_z. Sapphire is an example of such material, as well as quartz or calcite.
- ***Biaxial***: These media have three independent elements. This is the case of materials such as mica, gypsum or topaz.

4.3 Wave propagation in anisotropic media

One of the main consequences when dealing with anisotropic media instead of isotropic media is that wave propagation is different. The change is due to the presence of an

extra term in the wave equation. In order to understand this, one must go back to Maxwell's equations where now the dielectric properties are described by the tensor, $\bar{\bar{\epsilon}}$ instead of the scalar ϵ:

$$\nabla \times \boldsymbol{D} = 0 \tag{4.7a}$$

$$\nabla \times \boldsymbol{B} = 0 \tag{4.7b}$$

$$\nabla \times \boldsymbol{E} = -\mu \frac{\partial \boldsymbol{H}}{\partial t} \tag{4.7c}$$

$$\nabla \times \boldsymbol{H} = \frac{\partial \boldsymbol{D}}{\partial t} \tag{4.7d}$$

We have assumed no charge nor current density i.e. $\rho_m = \boldsymbol{j}_m = 0$. We are mainly interested in the propagation of monochromatic plane waves. Therefore we are looking for solutions to Maxwell's equations of the form:

$$\boldsymbol{E} = \boldsymbol{E}_0 \, e^{i(\boldsymbol{k}\cdot\boldsymbol{r} - \omega t)} \tag{4.8}$$

Notice that the vector amplitudes $\boldsymbol{E}_0$ and $\boldsymbol{H}_0$ are space independent. This means that we are working with waves of constant polarization. Plugging this into the non-homogeneous equations in (4.7) we find:

$$\boldsymbol{k} \cdot \boldsymbol{D}_0 = 0 \tag{4.9a}$$

$$\boldsymbol{k} \cdot \boldsymbol{H}_0 = 0 \tag{4.9b}$$

$$\boldsymbol{k} \times \boldsymbol{E}_0 = \omega \mu \boldsymbol{H}_0 \tag{4.9c}$$

$$\boldsymbol{k} \times \boldsymbol{H}_0 = -\omega \boldsymbol{D}_0 \tag{4.9d}$$

Now, although we have a new set of modified Maxwell equations (3.1), we make the approximation that the coupling constant is small enough to not have any effect on the propagation of EM waves. From (4.9c) one can read the usual accompanying field $\boldsymbol{H} = \boldsymbol{H}_0 e^{i(\boldsymbol{k}\cdot\boldsymbol{r} - \omega t)}$. Also, the orthogonality relations between vectors for a well defined direction of propagation $\boldsymbol{k}$ become clear. In particular from (4.9a),(4.9b) and (4.9d) we see that $\boldsymbol{k}, \boldsymbol{D}$ and $\boldsymbol{H}$(and so, also $\boldsymbol{B}$) form a set of orthogonal vectors. From (4.9c) we see that so do $\boldsymbol{H}$, $\boldsymbol{E}$ and the Poynting vector $\boldsymbol{S} = \boldsymbol{E} \times \boldsymbol{H}$. Contrary to what happened in the isotropic case, $\boldsymbol{E}$ and $\boldsymbol{k}$ are no longer necessarily orthogonal.

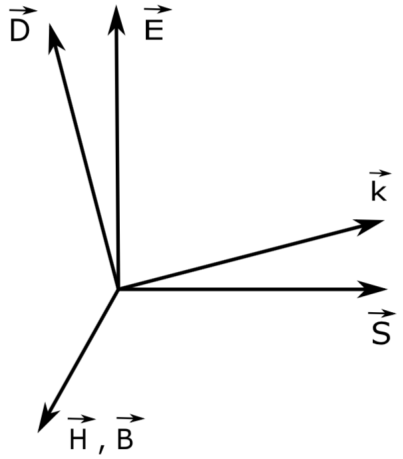

FIGURE 4.2: Representation of the general orientation of vectors of propagating plane wave.

Recall that we will be working with non-permeable media, in which case we always have $\mu = 1$. From the third and fourth equations in (4.9) we can derive the wave equation for anisotropic media:

$$(\boldsymbol{k} \cdot \boldsymbol{E_0})\boldsymbol{k} - k^2 \boldsymbol{E_0} = -\omega^2 \bar{\bar{\epsilon}} \boldsymbol{E_0} \tag{4.10}$$

For simplicity we express this in component form in the principal axes as:

$$\left(k^2 - n_j^2 \omega^2\right) E_{0,j} - (\boldsymbol{k} \cdot \boldsymbol{E}_0) k_j = 0 \tag{4.11}$$

where E_j, k_j and $n_j = \sqrt{\epsilon_j}$ are respectively the components of the electric field, propagation vector and refractive index associated with each of the principal axes. Notice that in contrast to what happened for isotropic media, now both electric field and $\boldsymbol{k}$ vector are not necessarily orthogonal. As a consequence the term $(\boldsymbol{k} \cdot \boldsymbol{E}_0)k_j$ doesn't vanish and we are left with a new wave equation.

The wave vector conveys two types of information. First, its absolute value is related to some refraction index, n and the frequency ω:

$$|\boldsymbol{k}| = \omega n \tag{4.12}$$

On the other hand the wave vector also gives us the perpendicular direction to the wave front $\boldsymbol{k} = \omega n \hat{\boldsymbol{\alpha}}$, where we introduce $\hat{\boldsymbol{\alpha}}$ as the unitary vector that specifies its direction. Thus, one can write the modified wave equation in component form for every index in the principal axes reference frame yielding a set of three linear equations:

$$E_x \left(\frac{\epsilon_x}{n^2} - \alpha_y^2 - \alpha_z^2\right) + \alpha_x\alpha_y\, E_y + \alpha_x\alpha_z\, E_z = 0 \tag{4.13a}$$

$$\alpha_y\alpha_x\, E_x + E_y \left(\frac{\epsilon_y}{n^2} - \alpha_x^2 - \alpha_z^2\right) + \alpha_y\alpha_z\, E_z = 0 \tag{4.13b}$$

$$\alpha_z\alpha_x\, E_x + \alpha_z\alpha_y\, E_y + E_z \left(\frac{\epsilon_z}{n^2} - \alpha_x^2 - \alpha_y^2\right) = 0 \tag{4.13c}$$

Specifying the direction of propagation $\hat{\boldsymbol{\alpha}}$ allows us to solve this eigenvalue problem for $\boldsymbol{E}$ and n.

4.4 Sapphire

The main goal of this document will be to describe the behaviour of sapphire, which will be the material used for the discs in our prototype and one of the strongest candidates for the final MADMAX experiment. Sapphire belongs to the class of the previously mentioned uniaxial media, for which the dielectric tensor has two independent components:

$$\epsilon_x = \epsilon_y = \epsilon_1 \qquad , \qquad \epsilon_z = \epsilon_2 \tag{4.14}$$

with $\epsilon_1 = 9.4$ and $\epsilon_2 = 11.8$ [14]. This means there are two axes in the principal axes reference frame corresponding to the dielectric constant ϵ_1, with an arbitrary direction on a plane orthogonal to a third axis, with dielectric constant ϵ_2 as sketched in Figure 4.3 .

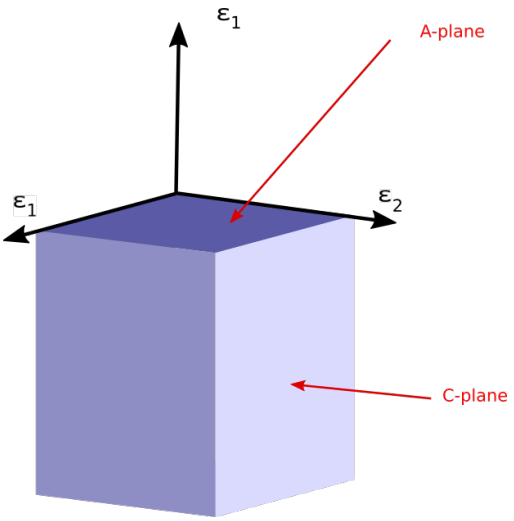

FIGURE 4.3: Representation of two of the possible cut planes for uniaxial media such as sapphire.

In practice, one grows a batch of sapphire and then makes a series of cuts of a certain thickness to form these discs. These cuts however, can be done in different directions with respect to the rincipal axes reference frame. Between the different kinds of crystal cut directions, possible for uniaxial media, there are two general ones we can consider. The first is a C-cut, where the plane of the disc is perpendicular to the direction of dielectric constant ϵ_2 and therefore with dielectric constant ϵ_1 in every direction of the disc. The second possibility is to do an A-cut, where along the cut plane the dielectric constant is ϵ_1 in some direction and ϵ_2 in an orthogonal one, and in its normal direction it's ϵ_1.

One of the issues, when using discs cut from such sapphire batch is that these cuts may have some imprecision and not be completely parallel to the A- and C-planes. These effects will be taken into account in the following chapter when we create a model to simulate the possible effects of anisotropic discs in a dielectric haloscope.

Chapter 5

MADMAX with Anisotropic Discs

In this chapter we describe how the axion induced electric field is affected by the anisotropy of the discs. In particular we will focus on the case of uniaxial discs such as sapphire. After this we will follow a parallel development to what was done in Chapter 3, in order to be able to simulate the system with uniaxial discs, imposing first the boundary conditions for a single interface, and generalising afterwards to the general multiple interface case. Then, using the transfer matrix formalism, we are able to solve the new set of equations and obtain the boost factor.

5.1 Anisotropic Axion Induced Electric Field

The anisotropy of the discs will affect the system in two different ways. First, as shown in Chapter 5, wave propagation is different in anisotropic media, to the extent that one must include a new term in the wave equation. Second, one must consider how the induced electric field is affected. In order to understand this second challenge, one has to go back to the Axion-Maxwell equations (3.1). As we saw in Chapter 5, the dielectric properties of anisotropic media are given by the tensor $\bar{\bar{\epsilon}}$. One can therefore rewrite (3.2b) as:

$$\boldsymbol{k} \times \hat{\boldsymbol{H}} + \omega \bar{\bar{\epsilon}} \hat{\boldsymbol{E}} = -g_{a\gamma} \omega \boldsymbol{B_e} \hat{a} \tag{5.1}$$

Taking into account once more that we are looking for CDM axions with non-relativistic speeds (i.e. $\boldsymbol{k} = 0$), and that $\bar{\bar{\epsilon}}$ is a symmetric tensor and therefore invertible, the axion induced electric field can be written as:

$$\boldsymbol{E}_a = -g_{a\gamma}\bar{\bar{\epsilon}}^{-1}\boldsymbol{B_e}a(t) \tag{5.2}$$

The only difference with the isotropic case in (3.7) is that now, since $\bar{\bar{\epsilon}}$ is a tensor, the electric field $\boldsymbol{E}_a$ and the external magnetic field $\boldsymbol{B}_e$ are no longer necessarily parallel. This complicates things in the sense that, added to the amplitude of the fields, one has to consider also their spatial direction. In other words, we go from a scalar to a vector description of the fields.

5.1.1 Boundary Conditions at an Interface

In the same way we did in Chapter 3, we look at the simplest case: a single interface between two different media. Since $\boldsymbol{E}_a$ can now have non-parallel components to the interface, one must extend the boundary conditions and include the orthogonal components to the interface. These are in particular:

$$\boldsymbol{D}_{\perp,1} = \boldsymbol{D}_{\perp,2} \qquad\qquad \boldsymbol{B}_{\perp,1} = \boldsymbol{B}_{\perp,2} \tag{5.3}$$

The magnetic field condition comes from Gauss' law for magnetism (3.1c) which is not affected by the presence of the axion. The displacement vector condition comes from Gauss' law for electricity (3.1a). The presence of the axion adds an effective charge density, and the boundary condition reads:

$$\boldsymbol{D}_{\perp,2} - \boldsymbol{D}_{\perp,1} = \rho - g_{a\gamma}\boldsymbol{B}\cdot\boldsymbol{\nabla}a \tag{5.4}$$

Since we consider that there are no net charges at the surface and that the axion is spatially homogeneous, meaning $\boldsymbol{k}_a = 0$, the gradient is $\boldsymbol{\nabla}a = 0$. The right hand side is therefore zero and we have the same boundary conditions as in classical electromagnetism.

Notice however, that these new boundary conditions are always fulfilled by the system. The magnetic field $\boldsymbol{B}_e$ is assumed to be parallel to the interface and has therefore no perpendicular components. The displacement vector $\boldsymbol{D}_a$ is given by:

$$\boldsymbol{D}_a = \bar{\bar{\epsilon}}\boldsymbol{E}_a = -g_{a\gamma}\boldsymbol{B}_e a(t) \tag{5.5}$$

and therefore always parallel to the interface. The most important consequence is that the induced EM radiation will have direction of propagation $\boldsymbol{k}$ perpendicular to the surface.

5.2 Two Reference Rrames

As shown in (4.6) the axion induced electric field $\boldsymbol{E}_a$ is best described by the principal axes reference frame. The magnetic field is however best described by a fixed frame, where the magnetic field is parallel to one of the axis. We will therefore generally have:

- **Fixed axes reference frame:** given by $x'y'z'$. It describes the position of the discs and the magnetic field. The $x'y'$ plane is the plane of the discs with y' the axis parallel to the magnetic field. The z'-axis represents the direction perpendicular to the discs.
- **Principal axes reference frame:** given by xyz. This is the principal axes reference frame of section 3.2 where the dielectric tensor is diagonal and therefore has fixed dielectric constant values in the x, y and z directions.

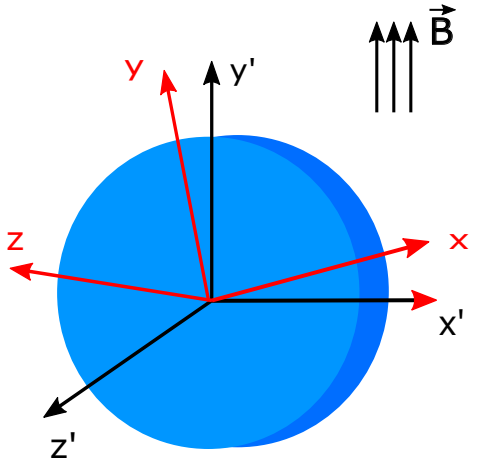

FIGURE 5.1: Representation of the relationship between the static reference frame $x'y'z'$, in black and the principal axes reference frame, xyz in red.

In order to obtain the different quantities in both reference frames we need to know how to relate one to the other. Since our goal is to describe sapphire we work directly with the assumption that the discs are uniaxial. Suppose then, that the z-axis corresponds to the direction with ϵ_2 dielectric constant value rotated by some angle ϕ with respect to the z'-axis. The other two axes (x- and y-axis) have the same dielectric constant value ϵ_1, and can therefore be defined in any direction on a plane perpendicular to z. Thus, one can always choose one of the axes to lay on the plane of the disc (this will be the

x-axis). The third axis (y-axis) is orthogonal to the previous two. The rotation between the x- and x'-axis is parametrized by an angle ψ. We find therefore, that one only needs ψ, and ϕ in order to relate the fixed and principal axes reference frame.

In practice one can understand ϕ as the miscut angle of the discs. On the other hand ψ represents not only the miscut angle but also the misalignment angle between the y axis and the direction of the magnetic field y'. If the cuts are done from the same sapphire batch it makes sense that the miscut angle is the same in every region. The misalignment angle however could vary from region to region and depends on experimental precision. This will be relevant in Chapter 6 when we make the simulation. For now however we treat these angles as region dependent ψ_r and ϕ_r.

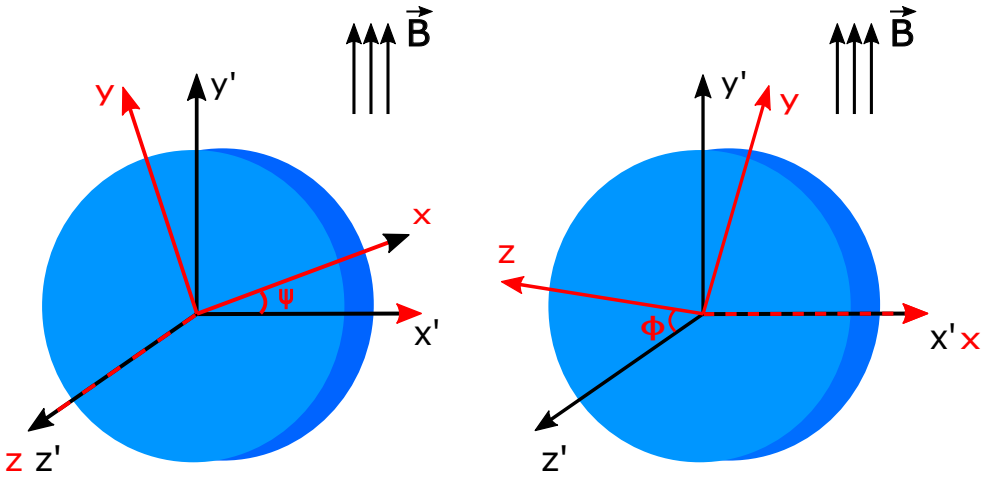

FIGURE 5.2: Representation of the fixed axes and the principal axes rotated with respect to each other. In the left figure the ϕ angle is zero. In the right the ψ angle representing the misalignement is zero.

Our identification of the z axis as the direction in which the dielectric constant is ϵ_2 represents the scenario of a crystal with a so called "C-cut". The other possible scenario is a disc with an "A-cut" in which case the z axis would have to be identified with the ϵ_1 dielectric constant. Notice however, that this can be achieved in our general case by shifting the angle ϕ by 90°.

5.2.1 Fields in the Principal Axes Frame

As mentioned before, the introduction of the principal axes reference frame is done in order to have a simple way of computing the axion induced electric field. In this frame we can therefore write:

$$E_{a,j} = -A_j E_0 \qquad , \qquad A_j \equiv \frac{1}{\epsilon_j}\frac{B_{e,j}}{B_{e,max}} \tag{5.6}$$

where we have $E_0 = g_{a\gamma} B_{e,max} a_0$ as the usual scale for the axion induced electric field, and $B_{e,max}$ the largest value of the external field. The index "j" represents the field component i.e. j=x,y,z. In order to obtain the magnetic field components in the principal axes reference frame $B_{e,j}$, one can use rotation matrices. In particular we use:

$$R_x(\psi) = \begin{pmatrix} \cos\psi & \sin\psi & 0 \\ -\sin\psi & \cos\psi & 0 \\ 0 & 0 & 1 \end{pmatrix} \qquad R_z(\phi) = \begin{pmatrix} 1 & 0 & 0 \\ 0 & \cos\phi & \sin\phi \\ 0 & -\sin\phi & \cos\phi \end{pmatrix} \tag{5.7}$$

A general vector $\boldsymbol{V'}$ in the fixed frame can then be written in terms of the principal axes frame as: $\boldsymbol{V} = R_z(\phi)R_x(\psi)\boldsymbol{V'}$. Hence, the magnetic field $\boldsymbol{B}_e$ in component form in the principal axes reference frame becomes:

$$B_{e,x,r} = B_{e,r}\sin\psi_r \tag{5.8a}$$
$$B_{e,y,r} = B_{e,r}\cos\psi_r\cos\phi_r \tag{5.8b}$$
$$B_{e,z,r} = -B_{e,r}\cos\psi_r\sin\phi_r \tag{5.8c}$$

allowing us to write for the A_j components:

$$A_{x,r} = \frac{1}{\epsilon_{x,r}}\frac{B_{e,r}}{B_{e,max}}\sin\psi_r \tag{5.9a}$$
$$A_{y,r} = \frac{1}{\epsilon_{y,r}}\frac{B_{e,r}}{B_{e,max}}\cos\psi_r\cos\phi_r \tag{5.9b}$$
$$A_{z,r} = -\frac{1}{\epsilon_{z,r}}\frac{B_{e,r}}{B_{e,max}}\cos\psi_r\sin\phi_r \tag{5.9c}$$

So far we've seen that disc anisotropy does have an effect on the axion induced electric field. In particular, it makes the field not necessarily parallel to the magnetic field. We've nevertheless been able to describe $\boldsymbol{E}_a$ in this new principal axes reference frame. We are still left however with the problem of wave propagation.

5.3 Wave Propagation inside the Discs

The propagation of waves in anisotropic media is also modified. In particular, as shown in Chapter 4, the wave equation has an extra term and one needs to solve the system (4.13) for our disc configuration. We have seen in section 5.1.1 that the $\boldsymbol{k}$ vector remains perpendicular to the interface. In the principal axes reference frame this means that it propagates in some direction on the yz plane given by $\hat{\boldsymbol{\alpha}} = (0, \sin\phi, \cos\phi)$. Substituting in our component form wave equation one finds:

$$E_x \left(\frac{\epsilon_x}{n^2} - 1\right) = 0 \tag{5.10a}$$

$$E_y \left(\frac{\epsilon_y}{n^2} - \cos^2\phi\right) + \sin\phi\cos\phi E_z = 0 \tag{5.10b}$$

$$\cos\phi\sin\phi E_y + \left(\frac{\epsilon_y}{n^2} - \sin^2\phi\right) E_z = 0 \tag{5.10c}$$

This equation has two solutions. The first one is the trivial:

$$n^2 = \epsilon_x\,,\; E_y = E_z = 0\,,\; E_x \neq 0 \implies n = \sqrt{\epsilon_x} \tag{5.11}$$

The other solution comes from imposing the determinant of the set of equations equal to zero yielding:

$$\frac{1}{n^2} = \left(\frac{\sin^2\phi}{\epsilon_z} + \frac{\cos^2\phi}{\epsilon_y}\right) \tag{5.12}$$

as an effective index of refraction, and substituting this in (5.10b):

$$\frac{E_z}{E_y} = -\frac{\epsilon_y}{\epsilon_z}\tan\phi \tag{5.13}$$

which gives us the direction of propagation as a relationship between the direction of E_y and E_z.

As we can see, we now have two propagation polarizations. Any solution of the modified wave equation is hence a superposition of a wave polarized in the x direction with a velocity related to a refractive index $n = \sqrt{\epsilon_x}$, and a wave propagating in some direction on the yz plane with a velocity related to the refractive index given by equation (5.12) and a direction given by (5.13).

5.4 General Uniaxial Setup

From here we can write the z' dependent, right and left moving electric fields of the induced EM radiation, in the x and yz plane directions (marked in the following with the subscript $\star$) for each region r:

$$E^R_{x,r}(z') = R_{x,r}e^{i\omega n_{x,r}\Delta z'} \quad , \quad E^L_{x,r}(z') = L_{x,r}e^{-i\omega n_{x,r}\Delta z'} \tag{5.14}$$

$$E^R_{\star,r}(z') = R_{\star,r}e^{i\omega n_{\star r}\Delta z'} \quad , \quad E^L_{\star,r}(z') = L_{\star,r}e^{-i\omega n_{\star r}\Delta z'} \tag{5.15}$$

where $\Delta z' = z' - z'_r$. These electric fields are accompanied by their respective magnetic fields which can be expressed in terms of the electric field as $H = nE$ thanks to Faraday's law:

$$H^R_{x,r}(z') = n_{x,r}R_{x,r}e^{i\omega n_{x,r}\Delta z'} \quad , \quad H^L_{x,r}(z') = -n_{x,r}L_{x,r}e^{-i\omega n_{x,r}\Delta z'} \tag{5.16}$$

$$H^R_{\star,r}(z') = n_{\star,r}R_{\star,r}e^{i\omega n_{\star,r}\Delta z'} \quad , \quad H^L_{\star,r}(z') = -n_{\star,r}L_{\star,r}e^{-i\omega n_{\star,r}\Delta z'} \tag{5.17}$$

where notice that the magnetic fields corresponding to right and left propagating waves have a different sign. This is necessary in order for the boundary conditions to be fulfilled. Notice also that $L_\star$ and $R_\star$ can be decomposed in terms of their y and z components. This, together with relation (5.13) allows us to rewrite everything in terms of the y field components:

$$L_{\star,r} = \sqrt{L^2_{y,r} + L^2_{z,r}} = L_{y,r}\sqrt{1+\beta_r^2} = L_{y,r}D_r \tag{5.18a}$$

$$R_{\star,r} = \sqrt{R^2_{y,r} + R^2_{z,r}} = R_{y,r}\sqrt{1+\beta_r^2} = R_{y,r}D_r \tag{5.18b}$$

where we have defined the quantity $D_r = \sqrt{1+\beta_r^2}$.

5.4.1 Imposing the Boundary Conditions

In each region the total electric and magnetic fields are a superposition of all the components discussed in the two previous sections i.e. axion induced electric field and left and right moving propagating waves. In contrast to what happened in the isotropic case, we now have to work with the complete set of vector field components:

$$\boldsymbol{E}_r^{tot}(z') = \boldsymbol{E}_{a,r} + \boldsymbol{E}_{x,r}^R(z') + \boldsymbol{E}_{x,r}^L(z') + \boldsymbol{E}_{\star,r}^R(z') + \boldsymbol{E}_{\star,r}^L(z') \tag{5.19}$$

$$\boldsymbol{H}_r^{tot}(z') = \boldsymbol{H}_{x,r}^R(z') + \boldsymbol{H}_{x,r}^L(z') + \boldsymbol{H}_{\star,r}^R(z') + \boldsymbol{H}_{\star,r}^L(z') \tag{5.20}$$

At this stage we are able to implement the continuity of $\boldsymbol{E}_{\parallel}$ and $\boldsymbol{H}_{\parallel}$. Since the ϕ and ψ angles that determine the relationship between principal axes and static frame of reference may be different in every region, and since in the setup of a dielectric haloscope, half of the regions are vacuum regions where the principal axes frame and the fixed frame are the same, we will always impose these boundary conditions in terms of the components of the fixed frame. The resulting boundary conditions are therefore given by the following four equations:

$$E_{y',r}(z'_{r+1}) = E_{y',r+1}(z'_{r+1}) \tag{5.21a}$$
$$E_{x',r}(z'_{r+1}) = E_{x',r+1}(z'_{r+1}) \tag{5.21b}$$
$$H_{y',r}(z'_{r+1}) = H_{y',r+1}(z'_{r+1}) \tag{5.21c}$$
$$H_{x',r}(z'_{r+1}) = H_{x',r+1}(z'_{r+1}) \tag{5.21d}$$

5.5 Transfer Matrix Formalism

In order to solve the previous set of equations and obtain the amplitude of the fields in any region we make use of the transfer matrix formalism in a similar way as in Chapter 3. The amplitudes in region r+1 are given in terms of the amplitudes in region r by:

$$\begin{pmatrix} R_{x,r+1} \\ L_{x,r+1} \\ R_{y,r+1} \\ L_{y,r+1} \end{pmatrix} = G_r P_r \begin{pmatrix} R_{x,r} \\ L_{x,r} \\ R_{y,r} \\ L_{y,r} \end{pmatrix} + E_0 S_r \begin{pmatrix} 1 \\ 1 \\ 1 \\ 1 \end{pmatrix} \tag{5.22}$$

where G_r, P_r and S_r are the following 4×4 matrices:

$$G_r = \frac{1}{2} \begin{pmatrix} \left[1 + \frac{n_{x,r}}{n_{x,r+1}}\right] \cos(\psi_{r+1} - \psi_r) & \left[1 - \frac{n_{x,r}}{n_{x,r+1}}\right] \cos(\psi_{r+1} - \psi_r) & \left[C_r + \frac{N_{\star,r}}{n_{x,r+1}}\right] \sin(\psi_{r+1} - \psi_r) & \left[C_r - \frac{N_{\star,r}}{n_{x,r+1}}\right] \sin(\psi_{r+1} - \psi_r) \\ \left[1 - \frac{n_{x,r}}{n_{x,r+1}}\right] \cos(\psi_{r+1} - \psi_r) & \left[1 + \frac{n_{x,r}}{n_{x,r+1}}\right] \cos(\psi_{r+1} - \psi_r) & \left[C_r - \frac{N_{\star,r}}{n_{x,r+1}}\right] \sin(\psi_{r+1} - \psi_r) & \left[C_r + \frac{N_{\star,r}}{n_{x,r+1}}\right] \sin(\psi_{r+1} - \psi_r) \\ -\left[\frac{1}{C_{r+1}} + \frac{n_{x,r}}{N_{\star,r+1}}\right] \sin(\psi_{r+1} - \psi_r) & -\left[\frac{1}{C_{r+1}} - \frac{n_{x,r}}{N_{\star,r+1}}\right] \sin(\psi_{r+1} - \psi_r) & \left[\frac{C_r}{C_{r+1}} + \frac{N_{\star,r}}{N_{\star,r+1}}\right] \cos(\psi_{r+1} - \psi_r) & \left[\frac{C_r}{C_{r+1}} - \frac{N_{\star,r}}{N_{\star,r+1}}\right] \cos(\psi_{r+1} - \psi_r) \\ -\left[\frac{1}{C_{r+1}} - \frac{n_{x,r}}{N_{\star,r+1}}\right] \sin(\psi_{r+1} - \psi_r) & -\left[\frac{1}{C_{r+1}} + \frac{n_{x,r}}{N_{\star,r+1}}\right] \sin(\psi_{r+1} - \psi_r) & \left[\frac{C_r}{C_{r+1}} - \frac{N_{\star,r}}{N_{\star,r+1}}\right] \cos(\psi_{r+1} - \psi_r) & \left[\frac{C_r}{C_{r+1}} + \frac{N_{\star,r}}{N_{\star,r+1}}\right] \cos(\psi_{r+1} - \psi_r) \end{pmatrix} \tag{5.23}$$

$$P_r = \begin{pmatrix} \exp\{i\delta_{x,r}\} & 0 & 0 & 0 \\ 0 & \exp\{-i\delta_{x,r}\} & 0 & 0 \\ 0 & 0 & \exp\{i\delta_{\star,r}\} & 0 \\ 0 & 0 & 0 & \exp\{-i\delta_{\star,r}\} \end{pmatrix} \tag{5.24}$$

$$S_r = \frac{1}{2}\begin{pmatrix} [(A_{r+1} - A_r)\sin\psi_{r+1} + (B_{r+1} - B_r)\cos\psi_{r+1}]_{2\times 2} & 0 \\ 0 & [(A_{r+1} - A_r)\cos\psi_{r+1} - (B_{r+1} - B_r)\sin\psi_{r+1}]_{2\times 2} \end{pmatrix} \tag{5.25}$$

The quantity $\delta_{i,r}$ in P_r is the optical thickness:

$$\delta_{i,r} = \omega n_{i,r}(z'_{r+1} - z'_r) \tag{5.26}$$

The derivation of these matrices is written in appendix A. There one can see how most quantities were defined. The ones in the G_r and S_r matrices are in particular:

$$N_{\star,r} = n_{\star,r}\sqrt{1+\beta_r^2} \quad , \quad C_r = \left(1 + \beta_r^2 \frac{\epsilon_{z,r}}{\epsilon_{y,r}}\right)\cos\phi_r \quad , \quad \beta_r = \tan\phi_r \frac{\epsilon_{y,r}}{\epsilon_{z,r}} \tag{5.27}$$

$$A_r = \frac{\cos\psi_r{}^2}{n_{\star,r}^2} + \frac{\sin\psi_r{}^2}{n_{x,r}^2} \quad , \quad B_r = \frac{\cos\psi_r \sin\psi_r}{n_{x,r}^2} - \frac{\sin\psi_r\cos\psi_r}{n_{\star,r}^2} \tag{5.28}$$

This result represents the main change from isotropic to anisotropic media. From here one can relate the amplitudes R and L of the external regions 0 and m by iteration, in the same way it was done for the isotropic case, yielding:

$$\begin{pmatrix} R_{x,m} \\ L_{x,m} \\ R_{y,m} \\ L_{y,m} \end{pmatrix} = T \begin{pmatrix} R_{x,0} \\ L_{x,0} \\ R_{y,0} \\ L_{y,0} \end{pmatrix} + E_0 M \begin{pmatrix} 1 \\ 1 \\ 1 \\ 1 \end{pmatrix} \tag{5.29}$$

with T the transfer matrix from regions 0 to m defined as:

$$T = T_0^m = G_{m-1}P_{m-1}G_{m-2}P_{m-2}\ ...\ G_1P_1G_0P_0 \tag{5.30}$$

and M:

$$M = \sum_{s=1}^{m} T_s^m S_{s-1} \tag{5.31}$$

which includes the contribution from the axion induced fields.

The major case comes from the limit where there are no incoming waves in the haloscope (i.e. $R_0 = L_m = 0$), allowing us to obtain the boost factor.

5.6 Anisotropic Boost Factor

For the limit $R_0 = L_m = 0$ the outgoing amplitudes are given by:

$$L_{y,0} = E_0 \left(\frac{T[2,2]M[4,\cdot] - M[2,\cdot]T[4,2]}{T[2,4]T[4,2] - T[2,2]T[4,4]} \right) \tag{5.32a}$$

$$L_{x,0} = E_0 \left(\frac{T[4,4]M[4,\cdot] - M[2,\cdot]T[2,4]}{T[2,4]T[4,2] - T[2,2]T[4,4]} \right) \tag{5.32b}$$

$$R_{x,m} = T[1,2]L_{x,0} + T[1,4]L_{y,0} + E_0 M[1,\cdot] \tag{5.32c}$$

$$R_{y,m} = T[3,2]L_{x,0} + T[3,4]L_{y,0} + E_0 M[3,\cdot] \tag{5.32d}$$

where we have made use of the following abbreviation: $M[i,\cdot] = \sum_{j=1}^{4} M[i,j]$ and where $T[i,j]$ is the matrix element of row i and column j. At this point we are ready to calculate the boost factor amplitude $\boldsymbol{\mathcal{B}}$ for a haloscope with uniaxial discs. Since now there are x-field and y-field components for the electric field there are three types of boost factor that can be defined. In case the antenna only detects polarizations parallel to the magnetic field this would be given by:

$$\mathcal{B}_{y,L} = \frac{L_{y,0}}{E_0} \qquad , \qquad \mathcal{B}_{y,R} = \frac{R_{y,m}}{E_0} \tag{5.33}$$

Notice that even though y pertains to the principal axes, in the $r = m$ region we are always in a vacuum region, which is isotropic and therefore has $\phi_m = \psi_m = 0$. In fact, in all $r = odd$ regions, the principal axes and fixed frame are the same. The second boost factor that can be defined, relates to the amplitude of the x component of the electric field:

$$\mathcal{B}_{x,L} = \frac{L_{x,0}}{E_0} \qquad , \qquad \mathcal{B}_{x,R} = \frac{R_{x,m}}{E_0} \tag{5.34}$$

Lastly, one can also define the total boost factor taking into account both x- and y-. To do so we go back to the definition of power boost factor in section 3.2.1 as the quantification of the amplification of the cycle-averaged power density with respect to a single mirror. The total power is therefore the squared sum of the x- and y- amplitudes. This gives us for the total power boost factor:

$$\mathcal{B}_{tot,L} = \frac{1}{E_0}\left(L_{y,0}^2 + L_{x,0}^2\right) \qquad , \qquad \mathcal{B}_{tot,R} = \frac{1}{E_0}\left(R_{y,m}^2 + R_{x,m}^2\right) \tag{5.35}$$

Chapter 6

1D Anisotropic Simulation

The boost factor is calculated in this section for a dielectric haloscope with sapphire discs. We analyse the two possible disc cuts with different misalignment angles for different number of discs and at different frequency ranges. Furthermore we present some consistency checks that bring some insight into the physical effects of having anisotropic discs.

6.1 General Sapphire Dielectric Haloscope Setup

In Chapter 5 we developed a model to include the effects of anisotropic discs in a dielectric haloscope. We are interested in particular in a dielectric haloscope with sapphire discs. Sapphire, as seen in chapter 4, is in the class of uniaxial media where in the principal axes reference frame the dielectric tensor is given by:

$$\bar{\bar{\epsilon}} = \begin{pmatrix} \epsilon_1 & 0 & 0 \\ 0 & \epsilon_1 & 0 \\ 0 & 0 & \epsilon_2 \end{pmatrix} \tag{6.1}$$

with $\epsilon_1 = 9.4$ and $\epsilon_2 = 11.8$. The sapphire crystal is grown and then cut into discs to be put in the haloscope in the even regions of figure 3.2. Physically there are two possible contributions to the misalignment between the principal axes and the fixed axes reference frames. The first one comes from miscut angles of the crystal. As we know from Chapter 4, one can make two types of cuts to the crystal:

- **C-cut**, where the axes of the principal axes are identified as: $\epsilon_x = \epsilon_y = 9.4$ and $\epsilon_z = 11.8$.
- **A-cut**, where the axes of the principal axes are identified as: $\epsilon_x = 11.8$ and $\epsilon_y = \epsilon_z = 9.4$.

This miscut of the crystal contributes to the misalignment between the principal axes reference frame and the fixed frame and is parametrized by the angle ϕ. The other source contributing to the misalignment between the two axes has to do with the orientation of the discs with respect to the magnetic field, and is parametrized by the angle ψ.

In Chapter 5 we developed the Transfer Matrix formalism to obtain the boost factor in a general setup of m regions r. We are interested however in a particular system where we have:

- A mirror in region $r = 0$, with dielectric constant $\epsilon = \infty$.
- Vacuum in every odd region ($r = 1, 3, ...m$), with dielectric constant $\epsilon = 1$.
- Sapphire discs in every even region ($r = 2, 4, ...m - 1$), with dielectric tensor in the principal axes frame $\bar{\bar{\epsilon}} = diag(\epsilon_1, \epsilon_1, \epsilon_2)$, and miscut and misalignment angles ϕ_r and ψ_r.

The simulation is done in 1D, meaning we assume that the discs are infinite in area. The only parameters are therefore, the spacing between the discs, which are optimized to get the desired broad band boost factor curve for a certain frequency, the thickness of said discs, and the ϕ and ψ angles in each region.

One can now imagine, that making cuts from the same sapphire crystal will give the same miscut angle for every disc. Hence, ϕ_r can be treated as having the same value ϕ for every even region. The misalignment angle ψ however, depends on how one positions the discs and can therefore have different values in every odd region. The most one can do is set a maximum precision angle. Taking the optimized disc positions for an isotropic configuration we can see what the effects of disc anisotropy with miscut and misalignment angles are for the boost factor curve. In particular, we can get the three boost factor curves introduced in section 5.6 i.e. total boost, x-boost and y-boost.

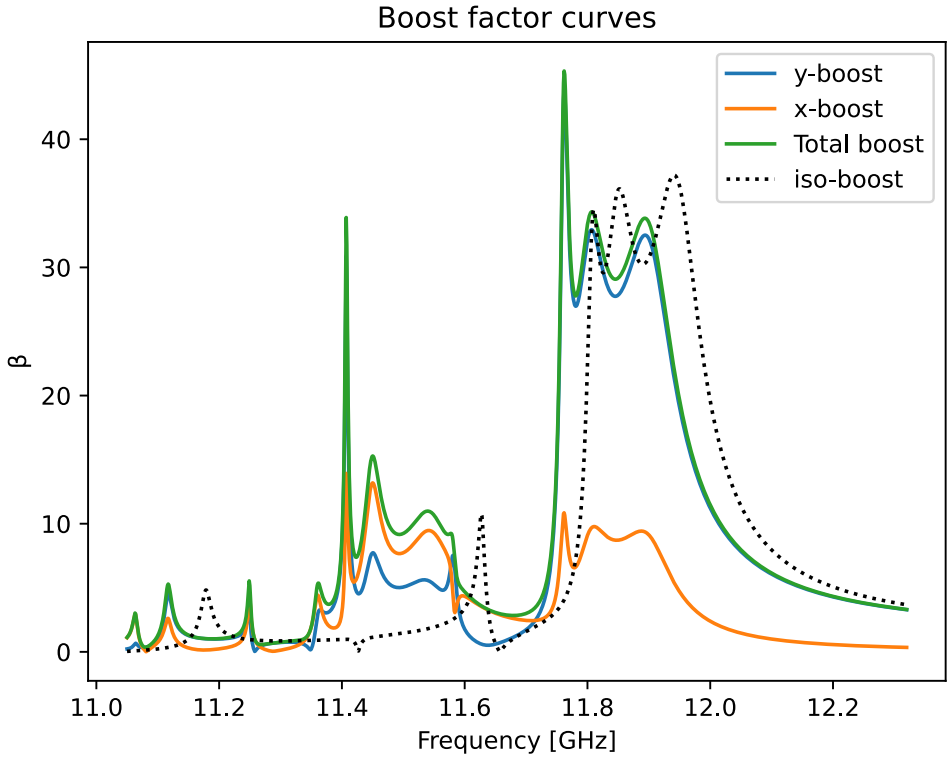

FIGURE 6.1: Example of the boost factor curves one can obtain with the transfer matrix formalism for anisotropic media, compared to the isotropic case.

6.2 Angle Span

An interesting exercise to understand the effect of anisotropy in the system is to vary the parameters ϕ and ψ for the same disc spacing. In particular one can study what happens when performing an angle span from 0° to 90° both for the ψ and ϕ angles. This also serves as a consistency check of the model since both the 0° and 90° are limits where one returns to the isotropic case.

6.2.1 C-cut Span

The first case we can study is that of a booster with c-cut discs. Keeping the ψ angle fixed at $\psi = 0°$ for all the discs in the booster, and rotating the ϕ angle from 0° to 90°, represents effectively a change of dielectric constant between $\epsilon = 9.4$ to $\epsilon = 11.8$, with the refractive index (and therefore dielectric constant given by (5.12)). Furthermore, the axion induced electric field will only have components along the yz plane.

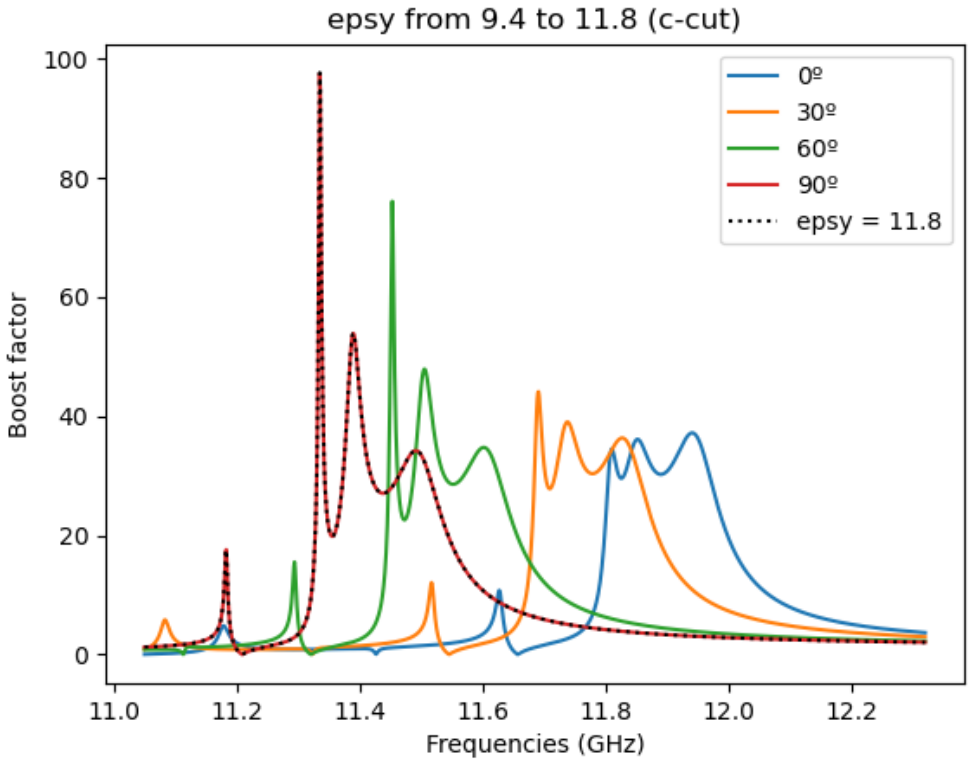

FIGURE 6.2

As we can see in Figure 6.2 the boost factor curve moves to a range of lower frequencies, and at $\phi = 90°$ the boost factor coincides with the boost factor for a dielectric constant $\epsilon = 11.8$, meaning that the correct isotropic limit is achieved.

6.2.2 A-cut Span

The second case one can study is that of a booster with a-cut discs. Performing a span from $\psi = 0°$ to $\psi = 90°$ while leaving $\phi = 0°$, represents effectively a change of dielectric constant from $\epsilon = 9.4$ to $\epsilon = 11.8$. The result in figure 6.3 shows us two things. First one can see that in the $\psi = 90°$ the boost factor curve coincides with the curve for a dielectric constant $\epsilon = 11.8$. This is as expected since changing the angle ψ effectively brings the dielectric constant from $\epsilon = 9.4$ to $\epsilon = 11.8$.

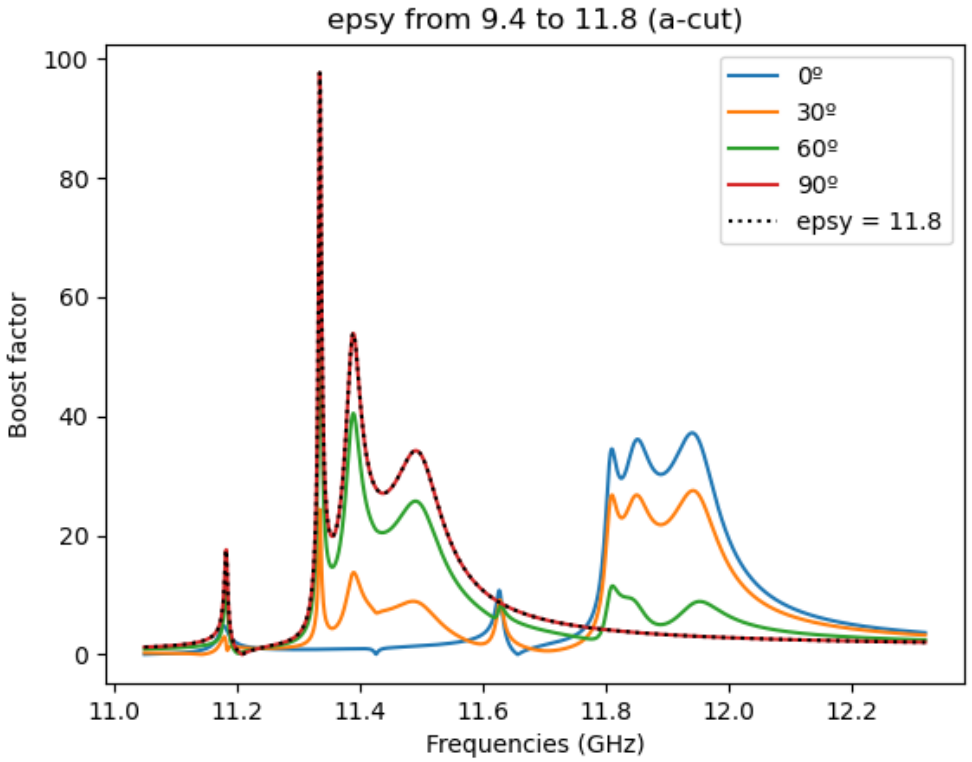

FIGURE 6.3: Span for 20 a-cut Sapphire discs with $\phi = 0°$ and $\psi = 0°$ to $\psi = 90°$.

The second thing to notice is the way in which the boost factor curve changes as we increase the value of ψ. For the extreme angles one gets a higher boost at different frequencies. In the intermediate angles however it's as if the booster stimulates both regions but not as efficiently. This is due to the fact that we are effectively looking at two polarizations in the x- and y- direction with two different effective dielectric constants.

6.3 Anisotropy Effects on Realistic Settings

In a realistic setting we don't expect to have miscut angles of more than 5°. In Figures 6.4 and 6.5 we study the effects of anisotropy for $\phi = 5°$ in a dielectric haloscope with twenty discs both for A-cut and C-cut discs at different frequency ranges. Each curve represents a setup where the misalignment angle ψ takes a different random value $|\psi| < 0°, 10°, 20°, 30°$ for each disc.

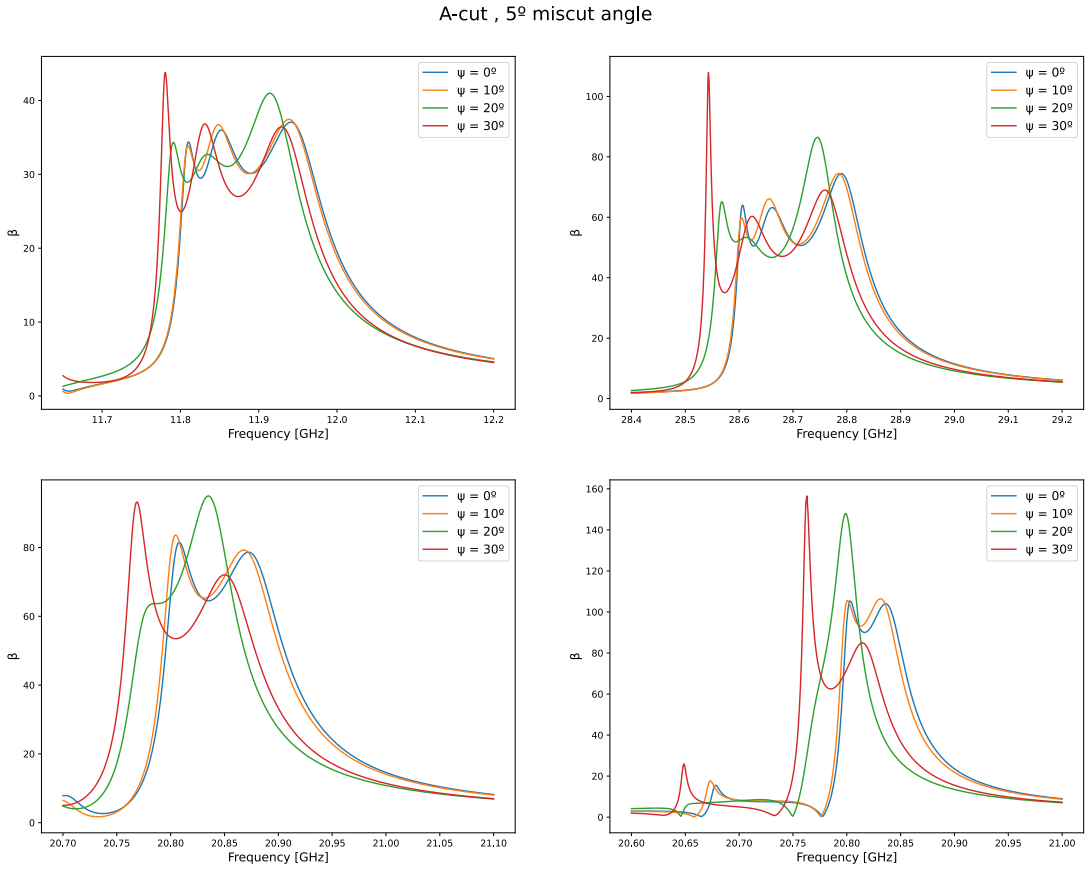

FIGURE 6.4: Boost factor curves at different frequency ranges for a dielectric haloscope with 20, 1mm A-cut sapphire discs and 5° miscut angle, and different randomized misalignment angles ψ

As we can see, for the case of a dielectric haloscope with A-cut discs the boost factor curve seems to preserve the isotropic behavior for misalignment angles lower than 20°. The situation changes considerably however, when one looks at the C-cut case. Here the contribution of the misalignment is close to none, and the boost factor preserves the isotropic shape even for misalignment angles of 30°. It seems therefore that if one can reduce the misalignment error to values lower than $\psi = 10°$, the anisotropy of the discs will not have a big affect on the shape of the boost factor for neither of the disc cuts.

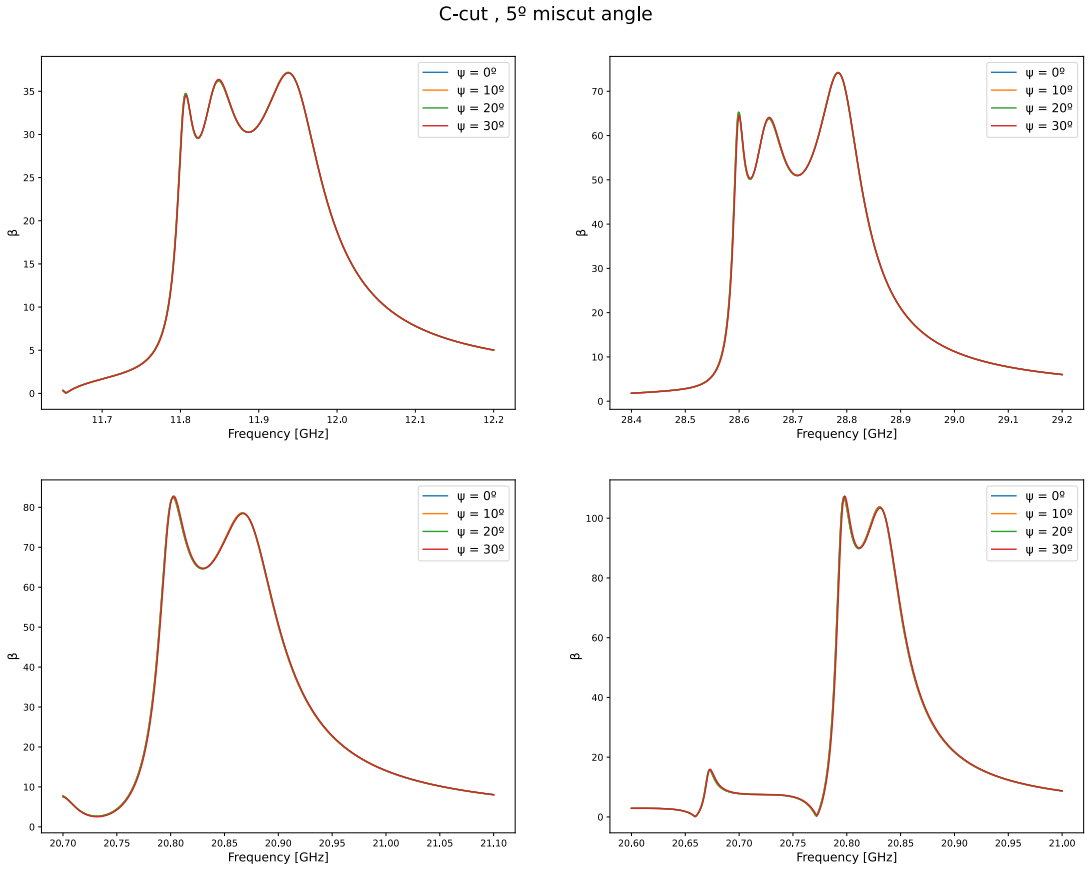

FIGURE 6.5: Boost factor curves at different frequency ranges for a dielectric haloscope with 20, 1mm C-cut sapphire discs and 5° miscut angle, and different randomized misalignment angles ψ

6.4 Random Misalignment Effects

The simulations are done by randomizing the misalignment angles ψ. We would therefore like to see how different disc randomization angles affect the boost factor curve from one random configuration of the angle ψ to another, while maintaining the same disc spacing. This was done for different numbers of discs. The results show that for a booster with a higher number of discs the boost factor curve varies much more for different random configurations of the misalignment angle ψ. However, as was seen in the previous section this only starts happening for high misalignment angles over $\psi = 7°$.

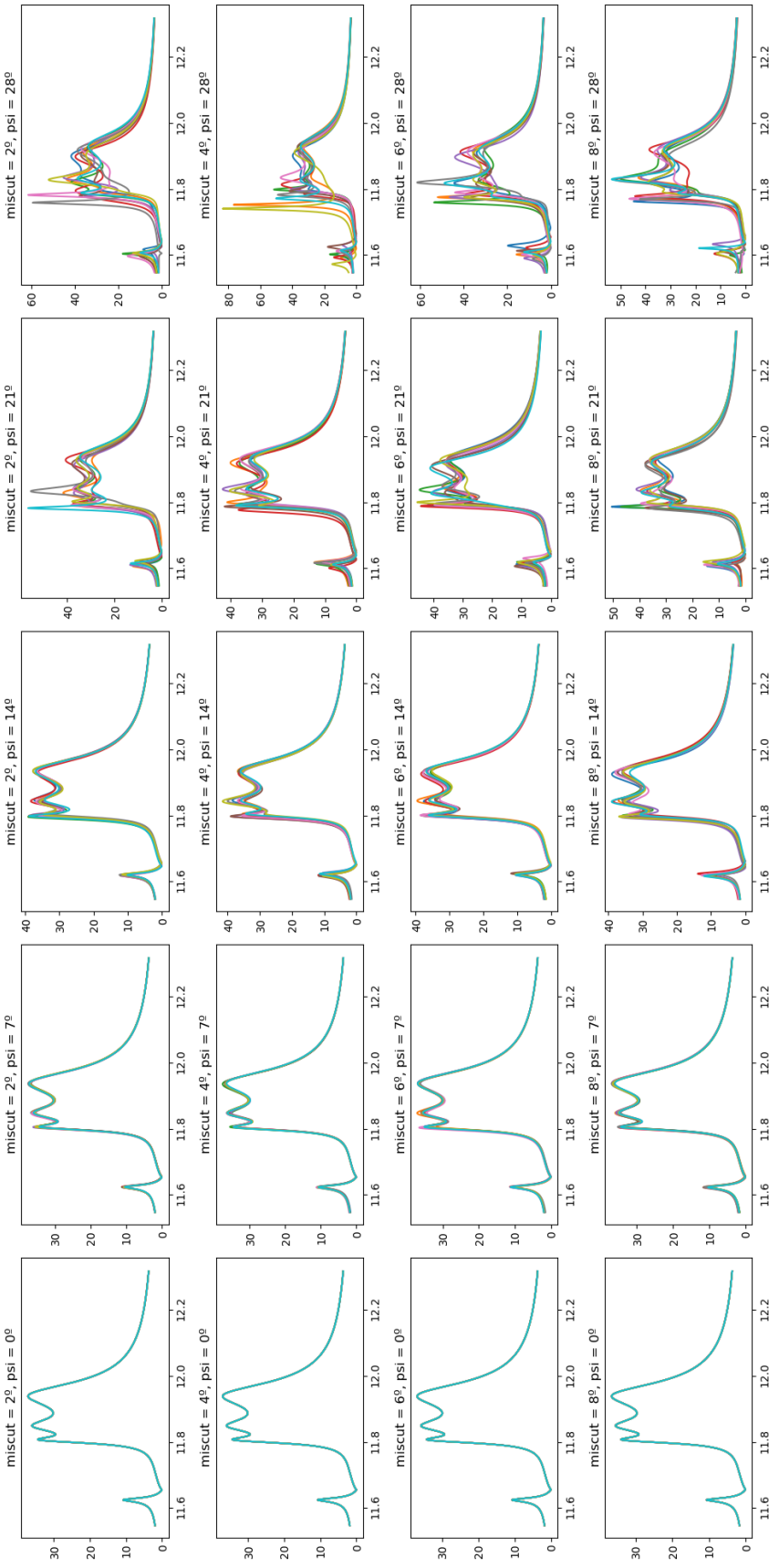

FIGURE 6.6: Different randomized ψ angle configurations for a 20 disc dielectric haloscope

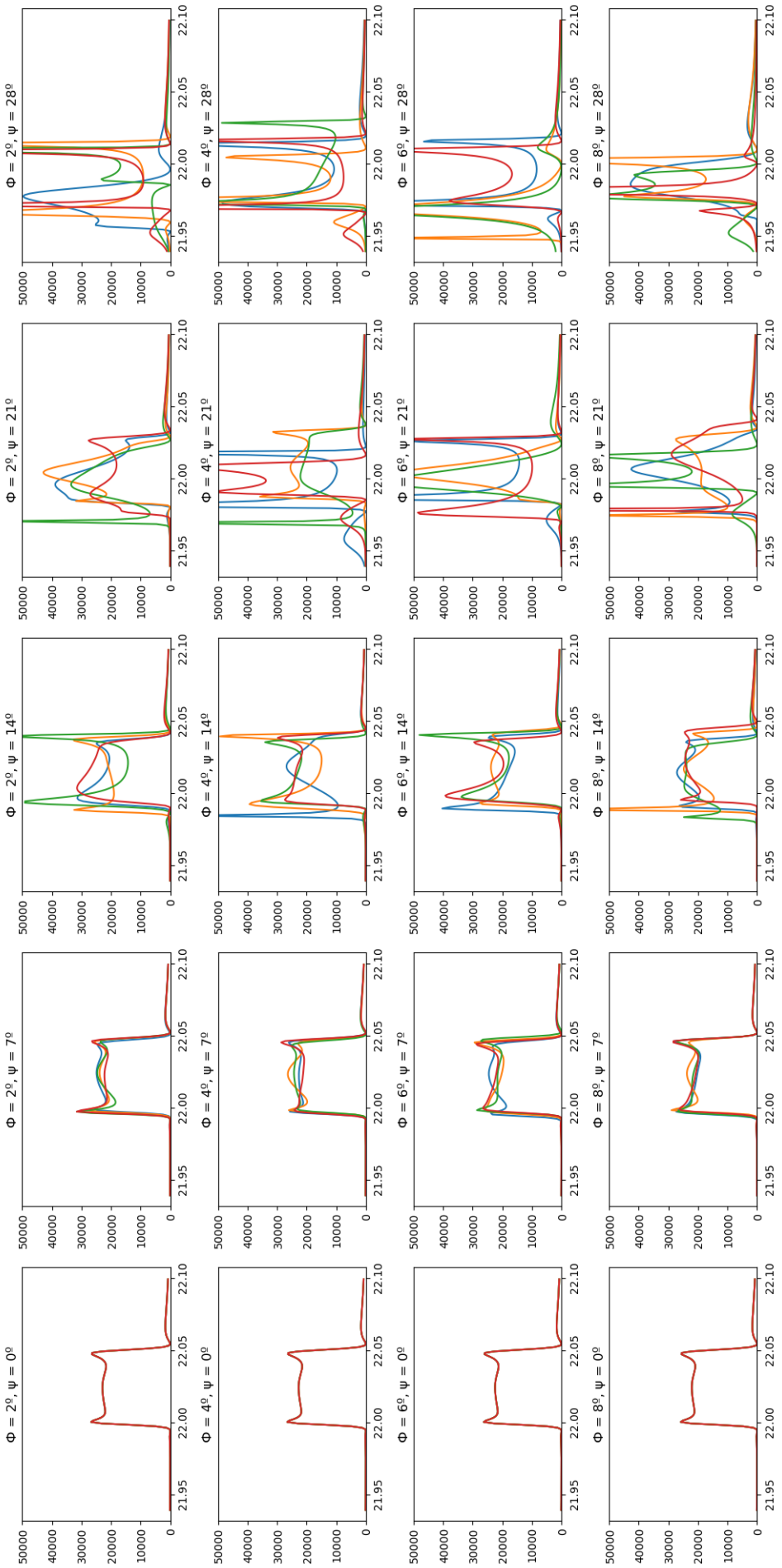

FIGURE 6.7: Different randomized ψ angle configurations for a 40 disc dielectric haloscope

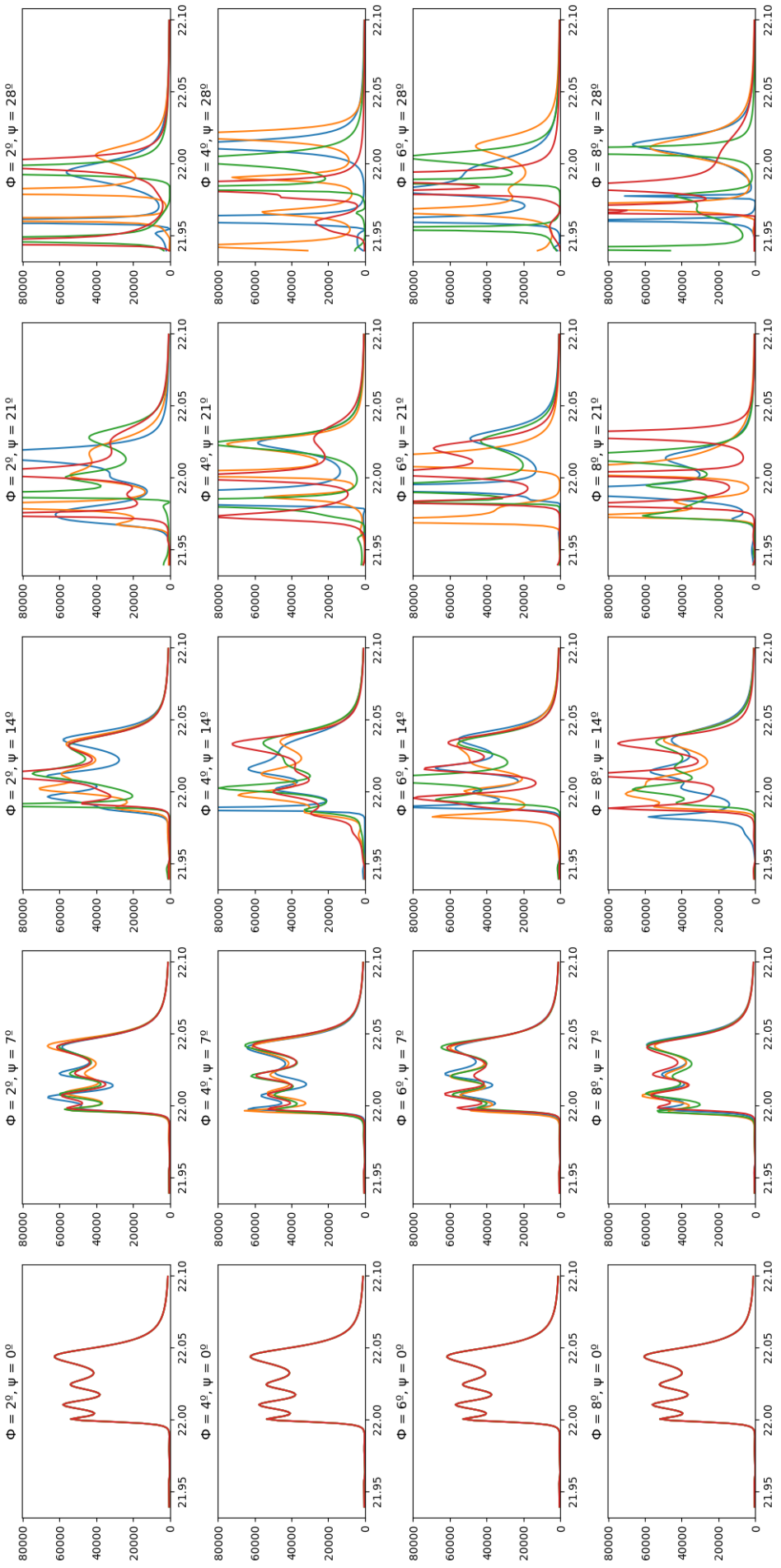

FIGURE 6.8: Different randomized ψ angle configurations for a 80 disc dielectric haloscope

Chapter 7

Conclusion

In this thesis, the current 1D simulations of a dielectric haloscope for the detection of dark matter axions, were adapted to include the possible effects of disc anisotropy. This was done by using the transfer matrix formalism, which went from being a 2×2 matrix equation for the isotropic case, to a 4×4 matrix equation for the anisotropic case. The particular scenario of a dielectric haloscope with sapphire discs was studied for the different A-cut and C-cut possibilities, with different miscut and misalignment angles. This was done by comparing the new predictions of the boost factor curve with the ones from the isotropic case.

The results show that indeed, disc anisotropy has a significant effect on the shape of the boost factor curve for big miscut and misalignment angles. For realistic settings however, where the miscut angle is not bigger than $5°$, these effects become very small, in particular for C-cut sapphire discs, where the effect is close to none. For A-cut discs, the biggest contribution to the modification of the boost factor curve with respect to the isotropic case, seems to come from the misalignment angle of the principal axes of the discs with respect to the magnetic field.

The number of discs present in the dielectric haloscope also seems to play a big factor in the effects of disc anisotropy on the boost factor. In particular, we saw that for a dielectric haloscope with larger number of discs, these effects become more relevant at smaller angles.

Appendix A

Calculation of the anisotropic Transfer Matrix

In this appendix we show the calculation of the G_r, P_r and S_r matrices from the boundary conditions in uniaxial anisotropic media. The explicit expression is obtained by substituting the total electric and magnetic fields (5.19) and (5.20) in each region, in the boundary conditions (5.21). The first step is to project the yz amplitudes of the Electric fields on to the $x'y'$ plane. For the EM waves this is:

$$\begin{aligned}
&\left(R_{yr}e^{i\omega n_{\star r}\Delta z'} + L_{yr}e^{-i\omega n_{\star r}\Delta z'}\right)\cos\phi_r - \left(R_{zr}e^{i\omega n_{\star r}\Delta z'} + L_{zr}e^{-i\omega n_{\star r}\Delta z'}\right)\sin\phi_r \\
&= R_{yr}\left(1+\beta_r^2\frac{\epsilon_z}{\epsilon_y}\right)\cos\phi_r\, e^{i\omega n_{\star r}\Delta z'} + L_{yr}\left(1+\beta_r^2\frac{\epsilon_z}{\epsilon_y}\right)\cos\phi_r\, e^{-i\omega n_{\star r}\Delta z'} \\
&= R_{yr}C_r\, e^{i\omega n_{\star r}\Delta z'} + L_{yr}C_r\, e^{-i\omega n_{\star r}\Delta z'}
\end{aligned} \tag{A.1}$$

where in the second line we have made use of equation (5.13) relating the E_y and E_z amplitudes. We have also defined the quantity: $C_r = \left(1+\beta_r^2\frac{\epsilon_z}{\epsilon_y}\right)\cos\phi_r$. The same type of projection can be done for the axion induced electric field:

$$\begin{aligned}
&A_{y,r}\cos\phi_r - A_{z,r}\sin\phi_r \\
&= \frac{1}{\epsilon_y}\frac{B_{e,r}}{B_{e,max}}\cos^2\phi_r + \frac{1}{\epsilon_z}\frac{B_{e,r}}{B_{e,max}}\sin^2\phi_r \\
&= \frac{1}{n_\star^2}\frac{B_{e,r}}{B_{e,max}}\cos\psi_r
\end{aligned} \tag{A.2}$$

This way the boundary conditions in the x' and y' axis are explicitly:

$$E_0(A_{r+1}-A_r)+\left(R_{x,r}e^{i\delta_{x,r}}+L_{x,r}e^{-i\delta_{x,r}}\right)\sin\psi_r+\left(R_{y,r}e^{i\delta_{\star,r}}+L_{y,r}e^{-i\delta_{\star,r}}\right)C_r\cos\psi_r=(R_{x,r+1}+L_{x,r+1})\sin\psi_{r+1}+(R_{y,r+1}+L_{y,r+1})\,C_{r+1}\cos\psi_{r+1} \tag{A.3a}$$

$$E_0(B_{r+1}-B_r)+\left(R_{x,r}e^{i\delta_{x,r}}+L_{x,r}e^{-i\delta_{x,r}}\right)\cos\psi_r-\left(R_{y,r}e^{i\delta_{\star,r}}+L_{y,r}e^{-i\delta_{\star,r}}\right)C_r\sin\psi_r=(R_{x,r+1}+L_{x,r+1})\cos\psi_{r+1}-(R_{y,r+1}+L_{y,r+1})\,C_{r+1}\sin\psi_{r+1} \tag{A.3b}$$

$$N_{\star,r}\left(R_{y,r}e^{i\delta_{\star,r}}-L_{y,r}e^{-i\delta_{\star,r}}\right)\sin\psi_r-n_{x,r}\left(R_{x,r}e^{i\delta_{x,r}}-L_{x,r}e^{-i\delta_{x,r}}\right)\cos\psi_r=N_{\star,r+1}\,(R_{y,r+1}-L_{y,r+1})\sin\psi_{r+1}-n_{x,r+1}\,(R_{x,r+1}-L_{x,r+1})\cos\psi_{r+1} \tag{A.3c}$$

$$N_{\star,r}\left(R_{y,r}e^{i\delta_{\star,r}}-L_{y,r}e^{-i\delta_{\star,r}}\right)\cos\psi_r+n_{x,r}\left(R_{x,r}e^{i\delta_{x,r}}-L_{x,r}e^{-i\delta_{x,r}}\right)\sin\psi_r=N_{\star,r+1}\,(R_{y,r+1}-L_{y,r+1})\cos\psi_{r+1}+n_{x,r+1}\,(R_{x,r+1}-L_{x,r+1})\sin\psi_{r+1} \tag{A.3d}$$

where $N_{\star,r}=n_{\star,r}D_r=n_{\star,r}\sqrt{1+\beta_r^2}$ and $\delta_{i,r}=\omega n_{i,r}(z'_{r+1}-z'_r)$ is the optical thickness, and the quantities A_r and B_r were defined as:

$$A_r=\left(\frac{\cos^2\psi_r}{n_{\star,r}^2}+\frac{\sin^2\psi_r}{n_{x,r}^2}\right)\qquad,\qquad B_r=\left(-\frac{\cos\psi_r\sin\psi_r}{n_{\star,r}^2}+\frac{\cos\psi_r\sin\psi_r}{n_{x,r}^2}\right) \tag{A.4}$$

The goal now is to express the amplitudes in region $r+1$ in terms of the amplitudes in region r. To do so we make the following manipulations of equations (A.3):

$$2R_{x,r+1}=\left[(a)+\frac{(d)}{n_{x,r+1}}\right]\sin\psi_{r+1}+\left[(b)-\frac{(c)}{n_{x,r+1}}\right]\cos\psi_{r+1} \tag{A.5a}$$

$$2L_{x,r+1}=\left[(a)-\frac{(d)}{n_{x,r+1}}\right]\sin\psi_{r+1}+\left[(b)+\frac{(c)}{n_{x,r+1}}\right]\cos\psi_{r+1} \tag{A.5b}$$

$$2R_{y,r+1}=\left[\frac{(a)}{C_{r+1}}+\frac{(d)}{N_{\star,r+1}}\right]\cos\psi_{r+1}-\left[\frac{(b)}{C_{r+1}}-\frac{(c)}{N_{\star,r+1}}\right]\sin\psi_{r+1} \tag{A.5c}$$

$$2L_{y,r+1}=\left[\frac{(a)}{C_{r+1}}-\frac{(d)}{N_{\star,r+1}}\right]\cos\psi_{r+1}-\left[\frac{(b)}{C_{r+1}}+\frac{(c)}{N_{\star,r+1}}\right]\sin\psi_{r+1} \tag{A.5d}$$

which making the following definition:

$$\gamma_r\equiv(A_{r+1}-A_r)\sin\psi_{r+1}+(B_{r+1}-B_r)\cos\psi_{r+1} \tag{A.6a}$$

$$\omega_r\equiv(A_{r+1}-A_r)\cos\psi_{r+1}-(B_{r+1}-B_r)\sin\psi_{r+1} \tag{A.6b}$$

lead to:

$$\begin{aligned}2R_{x,r+1}=E_0\gamma_r+e^{i\delta_{x,r}}\cos(\psi_{r+1}-\psi_r)\left[1+\frac{n_{x,r}}{n_{x,r+1}}\right]R_{x,r}+e^{-i\delta_{x,r}}\cos(\psi_{r+1}-\psi_r)\left[1-\frac{n_{x,r}}{n_{x,r+1}}\right]L_{x,r}\\+e^{i\delta_{\star,r}}\sin(\psi_{r+1}-\psi_r)\left[C_r+\frac{N_{\star,r}}{n_{x,r+1}}\right]R_{y,r}+e^{-i\delta_{\star,r}}\sin(\psi_{r+1}-\psi_r)\left[C_r-\frac{N_{\star,r}}{n_{x,r+1}}\right]L_{y,r}\end{aligned} \tag{A.7a}$$

$$\begin{aligned} 2L_{xr+1} = E_0\gamma_r + e^{i\delta_{xr}}\cos(\psi_{r+1}-\psi_r)\left[1-\frac{n_{xr}}{n_{xr+1}}\right]R_{xr} + e^{-i\delta_{xr}}\cos(\psi_{r+1}-\psi_r)\left[1+\frac{n_{xr}}{n_{xr+1}}\right]L_{xr} \\ +e^{i\delta_{\star r}}\sin(\psi_{r+1}-\psi_r)\left[C_r-\frac{N_{\star r}}{n_{xr+1}}\right]R_{yr} + e^{-i\delta_{\star r}}\sin(\psi_{r+1}-\psi_r)\left[C_r+\frac{N_{\star r}}{n_{xr+1}}\right]L_{yr} \end{aligned} \tag{A.7b}$$

$$\begin{aligned} 2R_{yr+1} = E_0\frac{\omega_r}{C_{r+1}} - e^{i\delta_{xr}}\sin(\psi_{r+1}-\psi_r)\left[\frac{1}{C_{r+1}}+\frac{n_{xr}}{N_{\star r+1}}\right]R_{xr} - e^{-i\delta_{xr}}\sin(\psi_{r+1}-\psi_r)\left[\frac{1}{C_{r+1}}-\frac{n_{xr}}{N_{\star r+1}}\right]L_{xr} \\ +e^{i\delta_{\star r}}\cos(\psi_{r+1}-\psi_r)\left[\frac{C_r}{C_{r+1}}+\frac{N_{\star r}}{N_{\star r+1}}\right]R_{yr} + e^{-i\delta_{\star r}}\cos(\psi_{r+1}-\psi_r)\left[\frac{C_r}{C_{r+1}}-\frac{N_{\star,r}}{N_{\star,r+1}}\right]L_{yr} \end{aligned} \tag{A.7c}$$

$$\begin{aligned} 2L_{y,r+1} = E_0\frac{\omega_r}{C_{r+1}} - e^{i\delta_{x,r}}\sin(\psi_{r+1}-\psi_r)\left[\frac{1}{C_{r+1}}-\frac{n_{x,r}}{N_{\star,r+1}}\right]R_{x,r} - e^{-i\delta_{x,r}}\sin(\psi_{r+1}-\psi_r)\left[\frac{1}{C_{r+1}}+\frac{n_{x,r}}{N_{\star,r+1}}\right]L_{x,r} \\ +e^{i\delta_{\star,r}}\cos(\psi_{r+1}-\psi_r)\left[\frac{C_r}{C_{r+1}}-\frac{N_{\star,r}}{N_{\star,r+1}}\right]R_{y,r} + e^{-i\delta_{\star,r}}\cos(\psi_{r+1}-\psi_r)\left[\frac{C_r}{C_{r+1}}+\frac{N_{\star,r}}{N_{\star,r+1}}\right]L_{y,r} \end{aligned} \tag{A.7d}$$

Which can at last be written in matrix form similarly to what is done for the isotropic case:

$$\begin{pmatrix} R_{x,r+1} \\ L_{x,r+1} \\ R_{y,r+1} \\ L_{y,r+1} \end{pmatrix} = G_r P_r \begin{pmatrix} R_{x,r} \\ L_{x,r} \\ R_{y,r} \\ L_{y,r} \end{pmatrix} + E_0 S_r \begin{pmatrix} 1 \\ 1 \\ 1 \\ 1 \end{pmatrix} \tag{A.8}$$

where now P_r, P_r and P_r are 4×4 matrices. The propagation matrix P_r is given by:

$$P_r = \begin{pmatrix} \exp\{i\delta_x, r\} & 0 & 0 & 0 \\ 0 & \exp\{-i\delta_x, r\} & 0 & 0 \\ 0 & 0 & \exp\{i\delta_\star, r\} & 0 \\ 0 & 0 & 0 & \exp\{-i\delta_\star, r\} \end{pmatrix} \tag{A.9}$$

G_r is:

$$G_r = \frac{1}{2}\begin{pmatrix} \left[1+\frac{n_{x,r}}{n_{x,r+1}}\right]\cos(\psi_{r+1}-\psi_r) & \left[1-\frac{n_{x,r}}{n_{x,r+1}}\right]\cos(\psi_{r+1}-\psi_r) & \left[C_r+\frac{N_{\star,r}}{n_{x,r+1}}\right]\sin(\psi_{r+1}-\psi_r) & \left[C_r-\frac{N_{\star,r}}{n_{x,r+1}}\right]\sin(\psi_{r+1}-\psi_r) \\ \left[1-\frac{n_{x,r}}{n_{x,r+1}}\right]\cos(\psi_{r+1}-\psi_r) & \left[1+\frac{n_{x,r}}{n_{x,r+1}}\right]\cos(\psi_{r+1}-\psi_r) & \left[C_r-\frac{N_{\star,r}}{n_{x,r+1}}\right]\sin(\psi_{r+1}-\psi_r) & \left[C_r+\frac{N_{\star,r}}{n_{x,r+1}}\right]\sin(\psi_{r+1}-\psi_r) \\ -\left[\frac{1}{C_{r+1}}+\frac{n_{x,r}}{N_{\star,r+1}}\right]\sin(\psi_{r+1}-\psi_r) & -\left[\frac{1}{C_{r+1}}-\frac{n_{x,r}}{N_{\star,r+1}}\right]\sin(\psi_{r+1}-\psi_r) & \left[\frac{C_r}{C_{r+1}}+\frac{N_{\star,r}}{N_{\star,r+1}}\right]\cos(\psi_{r+1}-\psi_r) & \left[\frac{C_r}{C_{r+1}}-\frac{N_{\star,r}}{N_{\star,r+1}}\right]\cos(\psi_{r+1}-\psi_r) \\ -\left[\frac{1}{C_{r+1}}-\frac{n_{x,r}}{N_{\star,r+1}}\right]\sin(\psi_{r+1}-\psi_r) & -\left[\frac{1}{C_{r+1}}+\frac{n_{x,r}}{N_{\star,r+1}}\right]\sin(\psi_{r+1}-\psi_r) & \left[\frac{C_r}{C_{r+1}}-\frac{N_{\star,r}}{N_{\star,r+1}}\right]\cos(\psi_{r+1}-\psi_r) & \left[\frac{C_r}{C_{r+1}}+\frac{N_{\star,r}}{N_{\star,r+1}}\right]\cos(\psi_{r+1}-\psi_r) \end{pmatrix} \tag{A.10}$$

And S_r:

$$S_r = \frac{1}{2}\begin{pmatrix} [(A_{r+1}-A_r)\sin\psi_{r+1} + (B_{r+1}-B_r)\cos\psi_{r+1}]_{2\times 2} & 0 \\ 0 & [(A_{r+1}-A_r)\cos\psi_{r+1} - (B_{r+1}-B_r)\sin\psi_{r+1}]_{2\times 2} \end{pmatrix} \tag{A.11}$$

References

[1] C. A. Baker, D. D. Doyle, P. Geltenbort, K. Green, M. G. D. van der Grinten, P. G. Harris, P. Iaydjiev, S. N. Ivanov, D. J. R. May, J. M. Pendlebury, J. D. Richardson, D. Shiers, and K. F. Smith, "Improved experimental limit on the electric dipole moment of the neutron," *Phys. Rev. Lett.*, vol. 97, p. 131801, Sep 2006.

[2] R. D. Peccei and H. R. Quinn, "CP conservation in the presence of pseudoparticles," *Phys. Rev. Lett.*, vol. 38, pp. 1440–1443, Jun 1977.

[3] F. Wilczek, "Problem of strong p and t invariance in the presence of instantons," *Phys. Rev. Lett.*, vol. 40, pp. 279–282, Jan 1978.

[4] S. Weinberg, "A new light boson?," *Phys. Rev. Lett.*, vol. 40, pp. 223–226, Jan 1978.

[5] G. G. di Cortona, E. Hardy, J. P. Vega, and G. Villadoro, "The qcd axion, precisely," *Journal of High Energy Physics*, vol. 40, 2016.

[6] R. Catena and P. Ullio, "A novel determination of the local dark matter density," *Journal of Cosmology and Astroparticle Physics*, vol. 2010, p. 004–004, Aug 2010.

[7] P. Sikivie, "Experimental tests of the "invisible" axion," *Phys. Rev. Lett.*, vol. 51, pp. 1415–1417, Oct 1983.

[8] A. Ringwald, "Axions and axion-like particles," 2014.

[9] I. G. Irastorza and J. Redondo, "New experimental approaches in the search for axion-like particles," *Progress in Particle and Nuclear Physics*, vol. 102, p. 89–159, Sep 2018.

[10] N. Du, N. Force, R. Khatiwada, E. Lentz, R. Ottens, L. J. Rosenberg, G. Rybka, G. Carosi, N. Woollett, D. Bowring, A. S. Chou, A. Sonnenschein, W. Wester, C. Boutan, N. S. Oblath, R. Bradley, E. J. Daw, A. V. Dixit, J. Clarke, S. R. O'Kelley, N. Crisosto, J. R. Gleason, S. Jois, P. Sikivie, I. Stern, N. S. Sullivan, D. B. Tanner, and G. C. Hilton, "Search for invisible axion dark matter with the axion dark matter experiment," *Phys. Rev. Lett.*, vol. 120, p. 151301, Apr 2018.

[11] A. J. Millar, G. G. Raffelt, J. Redondo, and F. D. Steffen, "Dielectric haloscopes to search for axion dark matter: theoretical foundations," *Journal of Cosmology and Astroparticle Physics*, vol. 2017, p. 061–061, Jan 2017.

[12] S. P. N. Knirck, *How To Search for Axion Dark Matter with MADMAX (MAgnetized Disk and Mirror Axion eXperiment)*. PhD thesis, Munich, Tech. U., 2020.

[13] G. Giusfredi, *Physical Optics: Concepts, Optical Elements, and Techniques*. UNITEXT for Physics, Springer International Publishing, 2019.

[14] E. Dobrovinskaya, L. Lytvynov, and V. Pishchik, *Sapphire: Material, Manufacturing, Applications*. Micro- and Opto-Electronic Materials, Structures, and Systems, Springer US, 2009.